



**HAL**  
open science

# Latitudinal Dependence of the Kelvin-Helmholtz Instability and Beta Dependence of Vortex-Induced High-Guide Field Magnetic Reconnection

Y. Vernisse, B. Lavraud, M. Faganello, S. Fadanelli, M. Sisti, F. Califano, S. Eriksson, D. Gershman, J. Dorelli, C. Pollock, et al.

► **To cite this version:**

Y. Vernisse, B. Lavraud, M. Faganello, S. Fadanelli, M. Sisti, et al.. Latitudinal Dependence of the Kelvin-Helmholtz Instability and Beta Dependence of Vortex-Induced High-Guide Field Magnetic Reconnection. *Journal of Geophysical Research Space Physics*, 2020, 125 (5), pp.e2019JA027333. 10.1029/2019JA027333 . hal-02886367

**HAL Id: hal-02886367**

**<https://hal.science/hal-02886367v1>**

Submitted on 2 Jul 2020

**HAL** is a multi-disciplinary open access archive for the deposit and dissemination of scientific research documents, whether they are published or not. The documents may come from teaching and research institutions in France or abroad, or from public or private research centers.

L'archive ouverte pluridisciplinaire **HAL**, est destinée au dépôt et à la diffusion de documents scientifiques de niveau recherche, publiés ou non, émanant des établissements d'enseignement et de recherche français ou étrangers, des laboratoires publics ou privés.

# 1 Latitudinal dependence of the Kelvin-Helmholtz instability and 2 beta dependence of vortex-induced high-guide field magnetic 3 reconnection

4  
5 Y. Vernisse<sup>1</sup>, B. Lavraud<sup>1</sup>, M. Faganello<sup>2</sup>, S. Fadanelli<sup>1,3</sup>, M. Sisti<sup>2,3</sup>, F. Califano<sup>3</sup>, S. Eriksson<sup>4</sup>, D. J. Gershman<sup>5,6</sup>, J.  
6 Dorelli<sup>5</sup>, C. Pollock<sup>5</sup>, B. Giles<sup>5</sup>, L. Avano<sup>5,6</sup>, J. Burch<sup>7</sup>, J. Dargent<sup>3</sup>, R. E. Ergun<sup>4</sup>, C. J. Farrugia<sup>8</sup>, V. Génot<sup>1</sup>, H.  
7 Hasegawa<sup>9</sup>, C. Jacquety<sup>1</sup>, I. Kacem<sup>1</sup>, R. Kieokaew<sup>1</sup>, M. Kuznetsova<sup>5</sup>, T. Moore<sup>5</sup>, T. Nakamura<sup>10</sup>, W. Paterson<sup>5</sup>, E.  
8 Penou<sup>1</sup>, T. D. Phan<sup>11</sup>, C. T. Russell<sup>12</sup>, Y. Saito<sup>9</sup>, J.-A. Sauvaud<sup>1</sup>, and S. Toledo-Redondo<sup>1</sup>

9  
10  
11 1 Institut de Recherche en Astrophysique et Planétologie, CNRS, UPS, CNES, Université Paul Sabatier, Toulouse,  
12 France

13 2 Laboratoire de Physique des Interactions Ioniques et Moléculaires, Université Aix-Marseille, Marseille, France

14 3 Physics department, University of Pisa, Pisa, Italy

15 4 University of Colorado / Laboratory for Atmospheric & Space Physics, Boulder, CO

16 5 NASA Goddard Space Flight Center, Greenbelt, MD

17 6 University of Maryland, College Park, MD

18 7 Southwest Research Institute, San Antonio, TX

19 8 University of New Hampshire, Durham, NH

20 9 Institute of Space and Astronautical Science, JAXA, Sagamihara, Japan

21 10 Space Research Institute, Austrian Academy of Sciences, Graz, Austria

22 11 Space Sciences Laboratory, Berkeley, CA

23 12 University of California, Los Angeles, CA

## 24 25 **Abstract**

26 We investigate both large- and small-scale properties of a Kelvin-Helmholtz (KH) event at the dusk flank  
27 magnetopause using Magnetospheric Multiscale (MMS) observations on 8 September 2015. We first use  
28 two types of 3D simulations (global and local) to demonstrate that MMS is close to the most KH unstable  
29 region, and so the occurrence of vortex-induced reconnection may be expected. Because they produce  
30 low-shear current sheets, KH vortices constitute a perfect laboratory to investigate magnetic  
31 reconnection with large guide field and low asymmetry. Recent works suggest that magnetic  
32 reconnection may be suppressed when a current sheet combines large guide field and pressure gradient  
33 (which induces a diamagnetic drift). We thus perform a statistical analysis of high-resolution data for the  
34 69 KH-induced low-shear magnetic reconnection events observed on that day. We find that the  
35 suppression mechanism is not at work for most of the observed reconnecting current sheets, as  
36 predicted, but we also find that almost all non-reconnecting current sheets should be reconnecting  
37 according to this model. This confirms the fact that the model provides a necessary but not sufficient  
38 condition for reconnection to occur. Finally, based on the same dataset, we study the latitudinal  
39 distribution of these magnetic reconnection events combined with global magnetospheric modelling. We  
40 find that reconnection associated with KH vortices occurs over a significant range of latitudes at the flank  
41 magnetopause. It is not confined to the plane where the growth rate is maximum, in agreement with  
42 recent 3D simulations.

43

## 44 **Keywords**

45 Earth's magnetosphere, space physics, Kelvin-Helmholtz instability, magnetic reconnection

46

## 47 **Keypoints**

- 48 • We use two types of global simulations to locate the KH unstable region at the magnetopause  
49 and determine its dynamics.
- 50 • We test the diamagnetic-drift reconnection suppression condition over 69 very-low shear  
51 current sheets and find an overall agreement.
- 52 • We report the broad latitudinal extent of magnetic reconnection locations triggered by KH  
53 vortices, consistent with bi-fluid 3D simulations.

54

## 55 **1 Introduction**

### 56 1.1 Kelvin-Helmholtz instability and magnetic reconnection

57 The Kelvin-Helmholtz instability, which develops in the presence of a sufficient velocity shear between  
58 two fluids, has been studied in space plasma physics for several decades [Chandrasekhar, 1961; Miura &  
59 Pritchett, 1982]. It has been extensively investigated using both observations [e.g. Fairfield et al., 2000;  
60 Nykyri et al., 2006; Foullon et al., 2010] and numerical simulations in different plasma regimes adopting  
61 fluid or kinetic approaches [e.g. Miura, 1995; Wilber and Winglee, 1995; Otto and Fairfield, 2000;  
62 Nakamura and Fujimoto, 2005; McNally et al., 2012]. The recent review paper by Faganello and Califano  
63 [2017] outlines past and recent works on the KHI. Recent advances have shown the importance of KH  
64 occurrence at the Earth's magnetopause [Kavosi and Reader, 2015; Lin et al., 2014] and many works  
65 have advocated for its role in plasma transfer at the magnetopause [e.g. Nykyri et al., 2017; Ma et al.,  
66 2017]. Through magnetic field entanglement and torsion, the KH instability provides favorable conditions  
67 for the triggering of magnetic reconnection. In particular, evidences for magnetic reconnection induced  
68 by a KH instability have been shown to occur within the vortices [Hasegawa et al., 2009; Eriksson et al.,  
69 2016; Li et al., 2016] as well as away from the vortices [Takagi et al., 2006]. Reconnection is notably  
70 triggered at the northern and southern edges of the vortices, caused by the propagation of the magnetic  
71 field line entanglement [Faganello et al., 2012a; 2012b; Borgogno et al., 2015; Vernisse et al., 2016].

72 Three types, or rather locations, for magnetic reconnection to occur have been identified in relation with  
73 KH waves and vortices. Type I magnetic reconnection [Liu and Hu, 1988; Chen et al., 1997; Knoll and  
74 Chacon, 2002; Nakamura et al., 2008] is defined as occurring at the compressed current sheet on the  
75 sunward face of the KH wave (or trailing edge). Type II reconnection takes place at the leading edge, in  
76 the developed vortices of the instability [Frank et al., 1996; Otto and Fairfield, 2000; Faganello et al.,  
77 2008; Nakamura et al., 2008], thanks to the interweaving of the magnetic field lines in the more  
78 turbulent plasma in this portion of the vortex [Stawarz et al., 2016]. The third type of reconnection is the  
79 mid-latitude reconnection scenario, as mentioned above to occur at the northern and southern edges of  
80 the vortices. It implies a reconnection process more distant from the equatorial waves or vortices,  
81 triggered by the propagation of the magnetic field line torsion in the vortices [Faganello et al., 2012;

82 *Borgogno et al., 2015*]. This scenario has been studied with data from THEMIS [*Faganello et al., 2014*]  
83 and MMS [*Vernisse et al., 2016*]. In any case, the KH instability either enhances the pre-existing  
84 magnetopause current sheet or creates new current sheets because of its own dynamics, finally leading  
85 to the development of very low shear magnetic reconnection events whose signatures may be detected  
86 by MMS.

87 Magnetic reconnection is a ubiquitous process that transforms magnetic energy into thermal and kinetic  
88 energies. It has been extensively studied in the literature [e.g., *Hesse et al., 2016*; and references  
89 therein]. For magnetic reconnection to occur, the change in plasma beta and magnetic shear angle  
90 across a current sheet plays a crucial role; it produces a diamagnetic gradient drift that may constitute a  
91 suppression mechanism for reconnection [*Swisdak et al., 2003; 2010*]. The vast amount of data gathered  
92 throughout the solar system has already largely constrained plasma parameter space for studying this  
93 suppression condition for magnetic reconnection. This condition has been tested with success in the  
94 solar wind [*Phan et al., 2010; Gosling & Phan, 2013*], the magnetosheath [*Phan et al., 2011*], the Earth's  
95 magnetopause [*Phan et al., 2013; Fuselier et al., 2017*] and Saturn's magnetopause [*Masters et al.,*  
96 *2012*]. However, for low beta plasmas ( $\beta < 0.1$ ), the drift-wave instability becomes prominent, and the  
97 diamagnetic suppression may be inefficient, as proposed by *Kobayashi et al.* [2014]. More recently, *Liu*  
98 *and Hesse* [2016] investigated diamagnetic suppression in the strong drift limit ( $\Delta\beta \gg 1$ ) using a  
99 moderate magnetic shear ( $\sim 90^\circ$ ). By separating the effect of the temperature and density in the pressure  
100 gradient term, they concluded that an anisotropy in the temperature allows the slippage of the electron  
101 motion relative to the magnetic flux, permitting magnetic reconnection to be maintained.

102 Owing to the properties mentioned above, KH waves can be used as a dedicated laboratory to study this  
103 suppression mechanism in the high guide field limit, which has only occasionally been investigated so far.  
104 We perform here a study of high-resolution data from the MMS mission [*Burch et al., 2015; 2016*]  
105 dedicated to the study of magnetic reconnection at the electron scale. Comparing a set of observed  
106 current sheets in between KH vortices, we find that the *Swisdak et al.* [2010] criterion properly predicts  
107 reconnecting current sheets, but not the non-reconnecting ones, suggesting this model provides a  
108 necessary but not sufficient condition for the triggering of magnetic reconnection.

109 The paper is organized as follows. In section 2 we analyze the KH events observed by MMS on 8  
110 September 2015 by means of the 3D global MHD simulation code BATS'R'US, provided by NASA's CCMC  
111 run on request system (<https://ccmc.gsfc.nasa.gov>). We then highlight the motion of the KH unstable  
112 plane relative to the IMF, as observed in earlier studies [*Farrugia et al., 1998*]. In section 3, we  
113 investigate the properties of magnetic reconnection inside the KH waves, and in particular the conditions  
114 for the suppression of reconnection by diamagnetic drift as theorized by *Swisdak et al.* [2003]. In section  
115 4, we combine the 3D MHD simulation and MMS data analysis to conclude on the latitudinal property of  
116 magnetic reconnection induced by the KH instability. Conclusions are given in section 5.

## 117 1.2 Diamagnetic suppression of magnetic reconnection

118 *Swisdak et al.* [2003] proposed that if the diamagnetic drift at a current sheet is faster than the Alfvén  
119 velocity associated with the reconnecting magnetic field component, then magnetic reconnection should  
120 be suppressed. In order to get such an expression, *Swisdak et al.* [2003] consider a 2.5D equilibrium  
121 where all fields are functions of two coordinates, perpendicular to the guide field. First, let us consider  
122 that the proper frame (LMN) is a well-determined, right-handed coordinate system, such that M  
123 corresponds to the guide field component, N is the component normal to the current sheet, and L is in

124 the direction of the reconnection outflow. Then, *Swisdak et al.* [2003] show that, at the null line, the ion  
 125 and electron diamagnetic drift velocities are given by:

$$126 \quad v_j^* = -q_j c \frac{\nabla P_j \times B}{en|B|^2} \Big|_{null\ line} = -q_j c \frac{\partial_N P_j}{enB_M} \Big|_{null\ line} \cong -q_j c \frac{\Delta P_j}{enL_{CS}B_M} \Big|_{null\ line},$$

127 where  $c$  and  $e$  are the speed of light and the Coulomb charge. The terms  $q$  and  $n$  stand for the charge  
 128 and density, and  $B$  is the magnetic field. The subscript  $j$  stands for ion or electron. The term  $\Delta P_j$   
 129 represents the thermal pressure jump across the current sheet.  $L_{CS}$  is the half-width of the current sheet.  
 130 In principle, if we assume the homogeneity of the thermal pressure and of the plasma properties in  
 131 general (i.e., the medium surrounding the x-point varies infinitesimally), the ansatz is valid. Let us focus  
 132 on the pressure variation term. Using the pressure tensor expressed in the LMN frame, the N component  
 133 of the pressure divergence reads:

$$134 \quad \partial_N P = \partial_L P_{LN} + \partial_N P_{NN} + \partial_M P_{NM}$$

135 Assuming that the off-diagonal terms are negligible, the diamagnetic drift for each species becomes

$$136 \quad v_j^* \cong -q_j c \frac{P_{j,NN}^{sh} - P_{j,NN}^{sp}}{enL_{CS}B_{M,null\ line}},$$

137 where the super-scripts “sh” and “sp” stand for magnetosheath and magnetosphere, respectively. To  
 138 express the suppression condition, we have to explicit the ion Alfvén velocity in the direction of the  
 139 exhaust (L):

$$140 \quad v_{A,L} = \frac{B_{L,asymptotic}}{\sqrt{4\pi m_i n_{i,null\ line}}}$$

141 Thus, the diamagnetic suppression criteria

$$142 \quad |v_i^*| + |v_e^*| > v_{A,L}$$

143 leads to

$$P_{j,NN}^{sh} - P_{j,NN}^{sp} > \frac{2L_{CS}}{d_{i,null\ line}} \frac{B_{M,null\ line} B_{L,asymptotic}}{8\pi} \quad (1)$$

144 where  $d_{i,null\ line}$  is the ion inertial length at the null line. Another way of expressing this condition uses the  
 145 plasma  $\beta$  on both side of the current sheet versus the magnetic shear angle  $\theta$ . In order to get such an  
 146 expression, from:

$$147 \quad \frac{P_{j,NN}^{sh} - P_{j,NN}^{sp}}{B_{M,null\ line}^2 / 8\pi} = \frac{2L_{CS}}{d_{i,null\ line}} \frac{B_{L,asymptotic}}{B_{M,null\ line}},$$

148 we finally get:

$$\Delta \beta_M > \frac{2L_{CS}}{d_{i,null\ line}} \tan \frac{\Theta}{2} \quad (2)$$

149 However, to obtain the last expression one needs to assume that the guide field is constant across the  
 150 current sheet. This last expression should be used carefully, in particular because the plasma  $\beta$  must be

151 derived with only the NN component of the pressure tensor, as well as only the M component of the  
 152 magnetic field for the magnetic pressure. Furthermore, one may argue that such a definition of a plasma  
 153  $\beta$  does not possess a proper physical meaning and can hardly be interpreted.

154 To complete the picture, the expression often used in the literature [e.g. *Gosling and Phan, 2013;*  
 155 *Masters, 2014; 2015*] is as follows

$$\Delta\beta = \frac{2L_{CS}}{d_i} \tan \frac{\theta}{2} , \quad (3)$$

156 where  $\Delta\beta$  stands for the difference between the total plasma  $\beta$  on the two sides of the current sheet  
 157 and  $\theta$  is the shear angle between the magnetic fields on the two sides of the current sheet (with no  
 158 specific component). This last equation, however, suffers from several simplifications of the suppression  
 159 model, as it does not take into account the exact quantities at stake here.

160 In the following section, we briefly investigate the validity of each formulation, and in particular the  
 161 validity of equation (3) with respect to the exact expression in equation (1).

162

## 163 2 Numerical simulations of the event

### 164 2.1 Global MHD simulation

165 In order to locate properly the Kelvin-Helmholtz instability at the magnetopause, and to compare with  
 166 observations, we requested runs of global MHD simulation codes from NASA's Community Coordinated  
 167 Modeling Center (CCMC) for the global magnetospheric models BATS'R'US [*Powell et al., 1999*] and  
 168 OpenGGCM [*Raeder et al., 2008*]. The simulations were initialized with OMNI data [*King and Papitashvili,*  
 169 *2005*], using the time interval during which the Kelvin-Helmholtz instability was observed by the MMS  
 170 satellites, on 8 September 2015 between 9:30 and 11:30 UT. We also ran simulations using THEMIS B  
 171 data, which was located in the solar wind during the whole event. The results are similar to those using  
 172 the OMNI data as shown here. MHD simulations use exclusively a constant IMF  $B_x$  at the solar wind  
 173 input. The results presented here thus do not properly account for the IMF cone angle. To mitigate this  
 174 limitation, we utilize a local 3D bi-fluid simulation in the next section to confirm the locations of KH  
 175 growth and reconnection.

176 Results of the simulation runs from BATS'R'US are presented in Figure 1. Results from OpenGGCM are  
 177 essentially similar and are not shown here. Figure 1a provides a three-dimensional representation of the  
 178 growth rate on the magnetopause surface, as derived from the output of the BATS'R'US simulation run.  
 179 We detect the magnetopause from the simulation data using the methodology detailed in Appendix A.  
 180 We compute the Kelvin-Helmholtz instability growth rate at the detected magnetopause using the  
 181 formula from *Chandrasekhar [1961]* for a discontinuous shear layer:

$$182 \left(\frac{\gamma}{k}\right)^2 = \frac{\rho_{sh}\rho_{sp}}{(\rho_{sh}+\rho_{sp})^2} \left( (\Delta\mathbf{U} \cdot \hat{\mathbf{k}})^2 - \frac{1}{\mu_0} \left( \frac{1}{\rho_{sh}} + \frac{1}{\rho_{sp}} \right) \left( (\mathbf{B}_{sh} \cdot \hat{\mathbf{k}})^2 + (\mathbf{B}_{sp} \cdot \hat{\mathbf{k}})^2 \right) \right) \quad (4)$$

183 where the term  $\Delta\mathbf{U}$  is the differential velocity between the magnetosphere and the magnetosheath. The  
 184 terms  $\rho$  and  $\mathbf{B}$  are the density and magnetic field, while the indices ('sh' and 'sp') stand for  
 185 magnetosheath and magnetosphere, taken at one Earth radius on each side of the identified  
 186 magnetopause. The distance to the magnetopause chosen to derive the growth rate is arbitrary, taking

187 into account the limited resolution of the simulation. We do not investigate the plasma penetration in  
188 the magnetosheath that appears in global MHD simulations [Li et al., 2009].

189 We use the velocity and magnetic field projected in the plane tangent to the magnetopause for each  
190 point. We search for  $\hat{\mathbf{k}}$  (normalized wave vector) such that it maximizes the above equation. The results  
191 are represented on a surface derived from the magnetopause model by Shue et al. [1997] (cf. Appendix  
192 A). Negative solutions of the growth rate are ignored and set to zero in Figure 1. The global amplitude of  
193 the growth rate is consistent with the amplitude derived from the MMS data, which give  $\frac{\gamma}{k} = 135 \text{ km/s}$   
194 [Eriksson et al., 2016]. It is worth noticing that the Chandrasekhar [1961] relation (4) neglects any effect  
195 due to the finite thickness of the velocity shear layer that reduces the growth rate and stabilizes short  
196 wavelengths [see Faganello and Califano, 2017, for further details]. This formula represents a first  
197 indication for the magnitude of the growth rate and shows the role of the velocity jump (projected on  
198 the wave vector direction) in driving the instability and the stabilizing role of the magnetic tension due to  
199 field line distortion when the magnetic field has a component along the flow shear.

200 In Figure 1a, the whole orbit of the MMS spacecraft on 8 September 2015 is plotted in blue, in the GSM  
201 coordinate system. We show the equator and the terminator with black lines. The Earth is at the center  
202 of the plot. A magnetic field line, derived from the simulation data, connected to the southern  
203 hemisphere on one side and connected to the solar wind on the other side is also displayed in red. We  
204 will refer to this magnetic field line in the following sections for context. Figures 1b and 1c (1d and 1e)  
205 show the growth rate (magnetic field shear) at the identified magnetopause at two simulated times,  
206 9:50:00 UT and 11:14:00 UT, respectively. The orientation of the IMF in the ( $Y_{\text{GSM}}, Z_{\text{GSM}}$ ) plane is  
207 represented with a white arrow in the plots and the position of the MMS spacecraft (from 9:30 UT to  
208 11:30 UT) is represented by black dots in Figures 1b and 1c, and by white dots in Figures 1d and 1e.

209 In Figure 1a, the three dimensional distribution of the growth rate at the magnetopause highlights the  
210 large-scale configuration of the KH unstable region at the magnetopause. In Figure 1b, we observe that  
211 although the IMF clock angle is low ( $10^\circ$ ), the dusk part of the KH unstable region is slightly shifted to the  
212 southern hemisphere, while the dawn side of the unstable region is shifted towards the northern  
213 hemisphere. In accord with Farrugia et al. [1998], this trend is more pronounced in Figure 1c for a clock  
214 angle of  $30^\circ$ . On the dusk side of the magnetopause, the most unstable region is shifted towards  
215 negative latitudes. This shift of the KH unstable region is consistent with the distribution of magnetic  
216 shear angle shown in Figure 1d and 1e. In Figure 1e, the MMS spacecraft were clearly cruising in the  
217 minimum magnetic shear angle region. These results highlight that the MMS spacecraft were well  
218 located to observe KH waves during the event, for these particular solar wind and IMF conditions.

## 219 2.2 Local 3D two-fluid simulation

220 We now analyze a local 3D two-fluid (Hall-MHD) simulation of the dusk flank to further demonstrate the  
221 KH development and vortex rolling-up during this event, confirming the fact that MMS satellites are well  
222 located and consistent with the occurrence of induced reconnection. This simulation starts from a  
223 modeled equilibrium, as in Fadanelli et al. [2018] that takes as asymptotic values (far away from the  
224 magnetopause) the plasma quantities measured during the event [Eriksson et al., 2016] in the boundary  
225 layer (outer magnetosphere) and in the magnetosheath plasma depletion layer (e.g., Wang et al., 2004),  
226 respectively. A three-dimensional rendering of the simulation is given in Figure 2b. In this simulation the  
227 linear KH growth rate, associated to the equilibrium, gradually decreases as  $|z|$  increases from  $|z| = 0$ ,

228 where  $z$  is the (signed) distance from the  $z = 0$  (coined equatorial plane hereafter), expressed in KH  
229 wavelength units ( $\lambda_{KH} \approx 12000 \text{ km}$  as given by the observed average period  $\approx 60\text{s}$  of KH oscillations  
230 and a phase-velocity  $\approx 200 \text{ km/s} \geq 1/2 \Delta U$ , with  $\Delta U \approx 350 \text{ km/s}$  being the observed velocity jump).  
231 This is observed in Figure 2a, where the growth rate drops at the box outer boundaries (located at  $z =$   
232  $\pm 4\lambda_{KH} \approx \pm 48000 \text{ km}$ ) to a third of its value at  $z = 0$ .

233 In Figure 2b, we show the simulation results at the beginning of the non-linear phase. KH vortices  
234 develop in a wide latitude range across the equatorial plane ( $z = 0$ ). Well-formed rolled-up structures are  
235 present from  $z = -\lambda_{KH} \approx -12000 \text{ km}$  to  $z = +3\lambda_{KH} \approx 36000 \text{ km}$ , as shown by the folded  
236 magnetopause, while the magnetopause at  $z = \pm 4\lambda_{KH} \approx \pm 48000 \text{ km}$  is nearly unperturbed. The KH  
237 development is asymmetric with respect to the equatorial plane, as expected when a flow-aligned  
238 component of the IMF is present [Fadanelli et al., 2018], even if all the other fields are symmetric. In the  
239 present case with  $B_{IMF} \cdot U_{SW} < 0$  the vortices develop more vigorously for  $z > 0$ , as expected. Although  
240 weaker for  $z < 0$ , they are still well formed at  $z = -\lambda_{KH} \approx -12000 \text{ km}$  where the MMS satellites are  
241 predicted to be if we refer to Figure 1b. More quantitatively, we estimate the value of the angle between  
242 the unperturbed magnetopause normal (the X axis in the simulation) and the actual normal measured in  
243 the simulations at the trailing (sunward facing) edge of the KH waves. This angle, which we term “trailing  
244 angle”, is shown in Figure 2c as a function of  $z$  at the beginning of the non-linear phase. The maximum  
245 value is around  $35^\circ$  and is located, as expected, in the upper part of the simulation domain where the  
246 vortices are most developed. In the bottom region, its value is smaller but at  $z = -\lambda_{KH} \approx -12000 \text{ km}$  it  
247 is still compatible with the values measured by MMS (as we will discuss in Section 4). Moreover, the  
248 folding time of the vortices in our simulation  $\tau_{fold} = \gamma_{KH,3D \text{ sim}}^{-1} \approx 92\text{s}$ , in dimensional units, is  
249 compatible with the time KH waves take to travel (at a phase-velocity  $\approx 200 \text{ km/s}$ ) from a longitude of  
250  $30^\circ$  to the MMS longitude. This fact suggests that KH vortices have time to fully develop before reaching  
251 the satellites.

252 Green regions in Figure 2b show where the magnetic field develops a component perpendicular to the  
253 local magnetopause as observed in the simulation in the non-linear phase. This normal magnetic field  
254 component, as defined and studied already in Faganello et al. [2012], would not develop in an ideal MHD  
255 evolution where the frozen-in condition is satisfied. This normal component was shown in Faganello et  
256 al. [2012] to be a clear signature that magnetic reconnection is occurring on the magnetopause, thereby  
257 the large-scale magnetic topology.

258 In summary, global simulations of the whole magnetosphere as well as a local simulation of the KH  
259 instability on the dusk flank magnetopause, indicate that the MMS satellites are in the proper location to  
260 detect well developed KH structures and, as a consequence, magnetic reconnection induced by the  
261 vortices. Furthermore, the local simulation suggests that reconnection proceeds on a wide latitude band  
262 as already observed in numerical simulations starting from a configuration similar to the present one  
263 [Fadanelli et al., 2018].

264

### 265 **3 MMS data analysis**

#### 266 **3.1 Event illustration**



267 On 8 September 2015, between 10:00 and 11:30 UT, the four MMS spacecraft sampled a long duration  
268 KH wave interval on the dusk side of the dayside magnetosphere [Eriksson *et al.*, 2016; Li *et al.*, 2016;  
269 Vernisse *et al.*, 2016]. We recall the context of the event in Figure 3. The clock angle and the cone angle  
270 shown in Figure 3a are from OMNI data [King and Papitashvili, 2005]. Figures 3b, 3c, and 3d display the  
271 magnetic field, ion bulk velocity, and ion plasma beta measured by the MMS1 spacecraft between 8:00  
272 and 13:00 UT. Although the IMF was mostly northward, the clock angle varied from a minimum of 15° (at  
273 10:45 UT) to a maximum of 40° (at 11:10 UT). In section 3.2, we perform a statistical analysis on 69  
274 magnetopause crossings observed during the event. Our statistics focuses on the trailing edge (also  
275 known as sunward edge) of the KH waves. This side of the KH wave has the thinnest current sheet and  
276 the distinction between the magnetospheric and magnetosheath plasma is easily made from the data. In  
277 order to determine whether the current sheet is reconnecting or not, we first perform a double Walén  
278 test (i.e., with positive and negative slopes each side of a possible ion jet; e.g. Phan *et al.*, 2004) on all the  
279 current sheets and verify if a reconnection jet is identifiable. We first base our work on the  
280 identifications provided by Eriksson *et al.* [2016], and revisit it with the newly available burst data (we  
281 provide all data in the supplementary material). Typical Walén tests that have been performed in order  
282 to identify potential reconnection jets are illustrated in Figures 3e to Figures 3n. Figures 3e and 3j show  
283 the magnetic field in a local LMN coordinate system as described in Eriksson *et al.* [2016] and Vernisse *et al.*  
284 [2016], which we recall here. We perform a minimum variance analysis [MVA, Sonnerup and Scheible,  
285 1998] on the current sheet to determine the L vector (the largest variance direction). The current sheet  
286 normal (N vector) is derived using the cross product of the magnetosheath and magnetosphere magnetic  
287 field. The M vector completes the coordinate system and is directed along the northward pointing guide  
288 field. Figure 3f and 3k present the L component of the velocity. Figure 3g and 3l show the electron pitch  
289 angle distributions, for energies between about ~274 eV and ~577 eV. Figure 3h and 3m show the ion  
290 plasma beta, while Figure 3i and 3n show the electron plasma beta.

291 The first and second black lines in Figure 3e to 3n delimit the main magnetopause current sheets. They  
292 are identified based on the decrease in plasma Beta (increase in density and decrease in temperature  
293 and magnetic field towards the magnetosheath), the decrease in suprathermal electron phase space  
294 density, and the magnetic field  $B_y$  variation (corresponding to a  $B_L$  variation), which is the typical main  
295 component varying at the trailing edge of KH waves at this location [e.g., Eriksson *et al.*, 2016]. Only the  
296 first event, in figures 3e to 3i, show typical signatures of a reconnection jet. This is corroborated by the  
297 Walén test in Figure 3f (albeit more qualitatively than quantitatively), where the L component of the  
298 velocity is plotted together with the variation of the Alfvén velocity as calculated from the magnetic field  
299 and density [see e.g. Phan *et al.*, 2004]. Clearly, in this first case, a jet is observed. In addition to  
300 identifying the signature of a jet in the ion bulk velocity, we searched for the possible presence of  
301 electron leakage from the magnetosphere to the magnetosheath [e.g., Fuselier *et al.*, 1995; 1997;  
302 Onsager *et al.*, 2001; Lavraud *et al.*, 2005; 2006]. Figure 3g shows a typical signature of such a leakage,  
303 identified by the increased electron flux in the field-aligned direction between the second and the third  
304 black vertical lines, outside the magnetopause in the magnetosheath boundary layer. This confirms that  
305 these field lines are open because of reconnection. By contrast, the current sheet delimited by the  
306 vertical black lines in Figure 3j to 3n presents no evident signatures of reconnection. There is no obvious  
307 jet between the black vertical lines in Figure 3k (there is a change in velocity across the current sheet,  
308 but this corresponds to a large-scale change induced by the vortex structure, from inside the MP to  
309 outside in the magnetosheath, rather than a jet). Correspondingly, we do not observe any electron  
310 leakage in Figure 3l after the current sheet.

311

### 312 3.2 Statistical analysis of current sheets

313 Here we analyze the 69 current sheets identified during the KH event observed by MMS1 on 8  
314 September 2015 (cf. supplementary material). Our analysis is as follows. We record the start and end  
315 times of each current sheet by hand. We define for each crossing a magnetosphere interval and a  
316 magnetosheath interval. The magnetosphere interval corresponds to three seconds of data before the  
317 start of the current sheet (e.g., three seconds on the left side of the first vertical black line for the case in  
318 Figures 3e to 3n). The magnetosheath interval corresponds to three seconds of data after the end of the  
319 current sheet (e.g. three seconds on the right side of the second vertical black line in Figure 3e to 3j). We  
320 derived the reference magnetosphere and magnetosheath parameters by averaging data on these  
321 intervals. In addition, we project both the velocity and magnetic field on the local LMN coordinate  
322 system defined above for each current sheet crossing.

323 We now confront MMS observations with the magnetic reconnection suppression model proposed by  
324 *Swisdak et al.* [2003] in Figure 4. In the first, second, and third columns of Figure 4 we confront Equations  
325 (1), (2), and (3), respectively, with our data analysis. For the derivation of Equation (1), we evaluate the  
326 pressure difference using the NN component of the pressure tensor expressed in the local LMN frame.  
327 Similarly,  $B_{L,asymptotic}$  (noted  $B_L$  in Figure 4 for the sake of concision) is the L component of the  
328 magnetic field evaluated as follow:  $B_{L,asymptotic} = \left| \frac{\langle B_{L,sheath} \rangle - \langle B_{L,sphere} \rangle}{2} \right|$ , where  $\langle \dots \rangle$  represents the  
329 mean operator (used on data from the magnetosphere and magnetosheath intervals as defined above).  
330 The term  $B_{M,null}$  (cf. introduction; noted  $B_M$  in Figure 4) is the M component of the magnetic field  
331 averaged over the current sheet traversal. The evaluation of Equation (2) requires the same quantities as  
332 Equation (1). We evaluate Equation (3) using the difference of the total plasma  $\beta$  averaged over the  
333 magnetosheath and magnetosphere intervals, respectively. The magnetic shear  $\theta$  is evaluated as:  $\theta =$   
334  $\arccos(b_{L,sheath} * b_{L,sphere} + b_{M,sheath} * b_{M,sphere})$ , where  $b_L = B_L/|B|$ . We derive all error bars by  
335 computing the standard deviation of each quantity during the 3-seconds intervals (and propagating it  
336 when required).

337 To confront our observations with the *Swisdak et al.* [2003] model, in a fashion similar to past studies  
338 [e.g., *Phan et al.*, 2013], we first need to determine whether the observed current sheets were  
339 reconnecting or not. We used three criteria for that purpose. As also explain in the previous section, the  
340 first criterion is the presence of a reconnection jet, visually identified by an ion velocity enhancement  
341 with consecutive positive and negative correlations with magnetic field changes, i.e., using the Walén  
342 test as illustrated in Figure 3 (first case). The second criterion for identifying reconnection is the  
343 identification of an electron boundary layer on the magnetosheath side of the current sheet, signaling  
344 the leakage of heated electrons along open field lines ensuing from reconnection. The directionality of  
345 heated leaking electrons (parallel or anti-parallel to the magnetic field) provides clues on the location of  
346 the X line relative to the spacecraft location (along the magnetic field) [e.g., *Fuselier et al.*, 1997; *Onsager*  
347 *et al.*, 2001; *Lavraud et al.*, 2006]. There is a straight link between the directionality of leaking electrons  
348 and the direction of the reconnection jet [*Vernisse et al.*, 2016]. Owing to the geometry of the event and  
349 the trajectory of the spacecraft, we expect to observe, on the magnetosheath side of the current sheet,  
350 electrons leaking parallel to the magnetic field when the jet is directed toward the  $-L$  direction (also seen  
351 as a decrease in the  $V_L$  component). Similarly, electrons leaking anti-parallel to the magnetic field in the  
352 magnetosheath are expected when the jet is directed along  $+L$  is observed; this corresponds to an

353 increase in the  $V_L$  component. The observation of a reconnection jet together with an electron leakage  
354 signature is thus deemed “consistent” if their directions are in the appropriate sense relative to the  
355 expected reconnection geometry.

356 Those identifications are presented in Figure 4. We categorize events following their likelihood of being  
357 reconnecting events. The first category shown in Figure 4a to 4c (‘jets & ebl consistent’) represents  
358 crossings where an ion jet and a consistent electron boundary layer are observed. The consistency  
359 between those two observations is illustrated in *Vernisse et al. [2016]* (Figure 3) and *Li et al. [2016]*  
360 (Figure 1), with the same configuration. The second category (‘jets & ebl present but not consistent’), in  
361 Figures 4d to 4f, is made of cases where both a jet and an electron layer were identified, but they were  
362 not consistent with each other (in terms of the directionality of the jet and the electrons, as explained  
363 above). The third category (‘only jets’), in Figure 4g to 4i, is based on events that present only a clear  
364 reconnection jet, and the fourth category (‘only ebl’), in Figure 4j to 4l, is made of cases where only an  
365 electron boundary layer was clearly observed. The fifth category (‘no jet and no ebl’), in Figure 4m to 4o,  
366 gathers crossings where neither a reconnection jet nor an electron boundary layer was observed. We  
367 provide a plot with all events in Figure 4p to 4r for sake of completeness. Equations (1), (2), and (3) are  
368 plotted in each Figure for three values of current sheet thicknesses,  $L_{eq} = 0.5, 1, \text{ and } 2 d_i$  (where  $d_i$  is  
369 the ion inertial length), in red, black, and blue, respectively. Points located under the curves should be  
370 non-reconnecting events according to the *Swisdak et al. [2003]* criterion. In brief, going down in each  
371 row of Figure 4, events are displayed such that they have less and less likelihood to be reconnecting  
372 events. In other words, there should be a tendency for all points in Figures 4a to 4c to be located above  
373 and/or to the left of the main curve, while points would, in principle, rather be located below and/or to  
374 the right of the curve in Figures 4m to 4o.

375 Several points have to be emphasized from Figure 4. The first thing to notice is the similarity of the  
376 results in the first and second column. This suggests that the hypothesis on the steady character of the  
377 guide field (see Section 1.1) across the current sheet is justified.

378 Secondly, the results in the third column (for Equation (3)) are different from the first and second  
379 columns. We notice that more points are located under the red curve in Figure 4c than in Figure 4a and  
380 4b. A similar behavior is noticeable in Figure 4l where several points stand under the black curve, while  
381 all points are above the black curve in Figures 4j and 4k. This means that Equation (3) tends to  
382 overestimate the suppression mechanism. The main difference comes from the derivation of the plasma  
383  $\beta$ , which in Equation (3) requires both the parallel thermal pressure and the  $B_L$  component of the  
384 magnetic field. For the observed events, the addition of the parallel pressure in the plasma  $\beta$  term plays  
385 the main role.

386 As mentioned by *Swisdak et al. [2010]*, the fact that the properties of a current sheet show conditions  
387 favorable for reconnection in the framework of this theory is a necessary but not sufficient condition for  
388 reconnection to occur. In that context, Equations 1 and 2 (Figure 4a and 4m) are in agreement with this  
389 assertion. However, Equation 3 is not, pointing to the need to use the proper component of the pressure  
390 tensor and magnetic field across the current sheet, when available. In this latter regard, we note that  
391 past studies (cf. introduction) typically did not have access to the full pressure tensor at sufficient  
392 resolution.

393 Thirdly, no clear trend is visible between the 5 classifications of events, and for all three models. As  
394 mentioned above one should expect a trend on the position of the points relative to the curve

395 depending on whether reconnection is ongoing or not. In particular, more and more points should move  
396 under the curve as we consider current sheets for which signatures of reconnection are less evident or  
397 even totally absent. We further discuss this lack of trend in the next sections.

398

### 399 **3.3 Possible limitations**

400 We must mention that our classification of the events may be biased in several ways. As we are studying  
401 small-scale current sheets, it is always possible that the reconnection jet or the electron boundary layer  
402 may be missed owing to proximity to the X line and/or insufficient time resolution. This is particularly  
403 true for the ion jets, which may not be observed if too close to the X line. We identified a few events that  
404 seem to possess an electron jet possibly consistent with a crossing close to the X-line. However, we leave  
405 the detailed analysis of such electron jets for future work. This limitation, in any case, is very unlikely to  
406 affect the electron boundary layer observations given the very high resolution of the MMS data (in  
407 particular as compared to past studies on the topic that were using much coarser resolution).

408 In addition, the compressed current sheet at the trailing edge of KH waves may be populated of  
409 numerous flux rope-type magnetic structures, as has been found in recent observations and simulations  
410 [Eriksson *et al.*, 2009; Nakamura *et al.* [2011; 2013; 2017a; 2017b]. This complexity of the current sheet  
411 may perturb the expected signatures both in terms of ion jet and electron boundary layer.

412

### 413 **3.4 Implications for existing models of magnetic reconnection suppression**

414 Despite these possible observational limitations, the lack of ordering of the reconnecting and non-  
415 reconnecting cases with respect to the theoretical curves (Figures 4a and 4m) suggests that the  
416 conditions provided by Equation (1) may not be sufficient in the specific regimes of nearly symmetric,  
417 high guide field reconnection such as here when induced by the KH instability. Recent studies have  
418 already revealed that the diamagnetic suppression may be mitigated in certain regimes. Kobayashi *et al.*  
419 [2014] investigated the diamagnetic suppression by means of gyrokinetic simulations, and found that in  
420 the regime of low plasma beta ( $\beta < 0.1$ ), the diamagnetic suppression is mitigated by the drift wave  
421 instability (which is prominent in that regime). A study by Liu and Hesse [2016] recently examined the  
422 regime of moderate magnetic shear ( $\sim 90^\circ$ ) and high beta difference ( $\sim 20$ ). In particular, they dissociated  
423 the role of the temperature and density gradients, which both account for the pressure gradient  
424 responsible of the suppression, and found that while the density gradient provides results similar to the  
425 global pressure gradient, the temperature gradient acts differently: a strong pressure gradient generated  
426 only by a strong temperature gradient does not suppress reconnection. Thus, disentangling the impact of  
427 the density gradient and the temperature gradient shall be performed in future work but falls out of the  
428 scope of the present paper. Neither of these studies, however, investigated the particular regime of low  
429 magnetic shear angle ( $< 60^\circ$ ) and moderate beta difference ( $\sim 1$ ). Further theoretical and observational  
430 studies are thus needed to determine whether a dedicated model is required in the high guide field  
431 reconnection regime.

432 We investigate in Figure 5 the possible role of the thickness of each current sheet. We derived the  
433 thickness of each current sheet using the mean of the N component of the ion bulk velocity, obtained  
434 with the cross-product method detailed earlier, over the current sheet crossing duration. We also used

435 the differential timing method [Harvey, 1998] to get the normal velocity and derive the current sheet  
436 thicknesses. Results from both methods are similar, thus we only present results using the cross product  
437 here. Figure 5a shows the distribution of the current sheet thickness for each category of event. Figure  
438 5b shows the cumulative distribution for each case to best demark the differences between these  
439 distributions. These show that the current sheet thicknesses are rather homogeneous, except for the  
440 events showing no clear signature of reconnection (no jet and no ebl). This is best observed in Figure 5b,  
441 with a marked difference between the cumulative distribution of non-reconnecting events (red curve)  
442 and the others. The average thicknesses of the distributions of the sets of events are  
443  $4.8 d_i$ ,  $5.66 d_i$ ,  $4.57 d_i$ ,  $6.24 d_i$ , and  $9.29 d_i$ , with standard deviations of  
444  $3.16 d_i$ ,  $2.39 d_i$ ,  $1.75 d_i$ ,  $5.76 d_i$ , and  $6.98 d_i$ , respectively for each category: “jet and ebl consistent”,  
445 “jet and ebl present but not consistent”, “only jets”, “only ebl”, and “no jet and no ebl”.

446 This finding is interesting. At first sight, it could suggest that these current sheets are non-reconnecting  
447 because of their overall larger thicknesses, a factor that is known to be important for reconnection to  
448 trigger [Priest & Forbes, 2000]. However, in the context of an asymmetric current sheet a small thickness  
449 in fact also implies a stronger gradient drift for the same asymptotic boundary conditions. Although  
450 somewhat counterintuitive, this observation in fact rather increases the inadequacy of our results with  
451 respect to the Swisdak et al. [2003] model. In other words, what this means is that in Figures 4m, 4n, and  
452 4o (for non-reconnecting current sheets) one should compare the distribution of points to the blue curve  
453 (or even more to the right, since a large thickness decreases the pressure gradient and ensuing gradient  
454 drift suppression effect) rather than to the black or red ones. Thus, in principle, almost all events should  
455 be reconnecting, or at least their conditions do not preclude reconnection from occurring.

456 Importantly, it must then be noted that if an event presents reconnection signatures and can be  
457 categorized as “reconnecting”, then the thickness would correspond to the thickness of the exhaust and  
458 not at all to the thickness of the initial current sheet before reconnection is triggered (while the latter is  
459 that relevant to the Swisdak et al. [2003] model). By contrast, for non-reconnecting current sheets, the  
460 measured thickness does correspond to the thickness that is relevant to the triggering of reconnection in  
461 the Swisdak et al. [2003] model. Again, in this context, according to Figures 4 and 5, most of the cases  
462 should in fact be reconnecting given the fact that for current sheet thicknesses equal or superior to 2  
463 inertial lengths the Swisdak et al. [2003] condition for reconnection is satisfied. However, we recall that  
464 this condition is necessary but not sufficient, as mentioned in Swisdak et al. [2016]. The present findings  
465 are thus consistent with the model.

466 Finally, it may also be noted that the rather thin, and homogeneously distributed, current sheet  
467 thicknesses of reconnecting events in Figure 4a, together with the fact that reconnecting current sheets  
468 are on average thinner than non-reconnecting ones, suggest that it is unlikely that we miss many thin  
469 reconnecting current sheets in our analysis. In other words, the temporal resolution of the MMS data  
470 should allow us not to miss a lot of reconnection jet.

471

#### 472 **4 Latitudinal dependence and three dimensional properties of the KH instability and induced** 473 **reconnection**

474 As shown in the literature by means of three-dimensional MHD [Ma et al., 2017] and multi-fluid  
475 simulations [Faganello et al., 2012; 2014, Borgogno et al., 2015], the limitation of the Kelvin-Helmholtz

476 instability to a two dimensional setup misses several key aspects of its development and ensuing  
477 topological properties. In Figure 6 we study the latitudinal distribution of the KH-induced reconnection  
478 events studied in section 3. As introduced in Section 2, we also performed a BATS'R'US simulation of this  
479 event, initialized with actual OMNI data. The same simulation using THEMIS B data as inflow conditions  
480 (sitting in Earth's upstream solar wind at that moment) showed no significant differences and is thus not  
481 presented.

482 For each data point of the MMS1 spacecraft location, we look for the maximum growth rate position on  
483 the same meridian in the global MHD simulation and measure the latitudinal distance of the spacecraft  
484 to this maximum growth rate. For that purpose, we use the time of each current sheet crossing from the  
485 MMS1 data to find the corresponding simulation output time to use, and to derive the location of the KH  
486 unstable region. The result of this analysis is presented in Figure 6a, where all current sheet crossings are  
487 categorized using the five types of signatures introduced in section 3.2.

488 Figure 6a presents each current sheet according to its distance to the maximum growth rate plane in  
489 terms of latitude angle plotted as a function of the angle between the normal to the unperturbed  
490 magnetopause (derived from the *Shue et al. [1997]* model) and the normal to each current sheet  
491 (derived using the cross-product method). We name the latter quantity "normal angle" for conciseness  
492 (it is similar to the trailing angle defined for the local simulation in Section 2.2). A range of 20° is covered  
493 in terms of spacecraft distance to the simulated maximum growth rate plane. The MMS spacecraft were  
494 thus cruising all the time fairly close to the maximum growth rate plane, but yet over a non-negligible  
495 range of latitudes and essentially on the southern side of the maximum growth rate plane. We also  
496 display in Figure 6a the directionalities of the ion jets with arrows, in accordance with the corresponding  
497 magnetic field geometry. Magnetic reconnection jets were observed southward and northward of the  
498 spacecraft, independently of their position relative to the most unstable plane, thus suggesting that the  
499 possible locations of reconnection triggering cover an extended latitudinal region relative to the  
500 maximum growth plane.

501 We note that events that are likely reconnecting (blue, cyan, and green points) appear somewhat less  
502 spread, in both normal angle and separation to the unstable region, than non-reconnecting cases  
503 (orange and red points). In terms of latitudinal spread, the computation of the standard deviation for  
504 each set of points gives 4°, 5.2°, 5°, 5.6°, and 5.7° from most likely reconnecting (blue) to less likely  
505 reconnecting (red) cases. This signals that the area of observation of reconnecting jets is less dispersed in  
506 latitude relative to the maximum growth rate plane, with a mean location 10° southward of that plane.  
507 Cases where no reconnecting jets are observed are found over a broader latitude range, suggesting no  
508 particular correlation with latitude. This property is consistent with a previous study [*Faganello et al.,*  
509 2012] showing that, in KH instabilities, reconnection occurs mostly away from the most unstable plane,  
510 due to the propagation of the twisting of the magnetic field.

511 Figure 6b presents time series of the latitude distance between the spacecraft and the maximum growth  
512 rate plane (red line) for each simulation output. Additionally, we show the IMF clock angle from OMNI  
513 (blue line) and the "normal angle" (black line). The distribution of this angle between the local current  
514 sheet normal and the unperturbed magnetopause shows that the vortices are broadly distributed over a  
515 range of latitudes, and seem not to be limited to the most unstable region. This suggests that the  
516 spacecraft are observing rather local signatures of reconnection, i.e., induced by the vortices (type I),  
517 rather than signatures of mid-latitude reconnection at the southern end of the unstable region.

518 However, as was recently shown in *Fadanelli et al.* [2018], when a non-negligible magnetic shear exists  
519 (non-purely parallel magnetic fields across the flank magnetopause; or in other words non-purely  
520 northward IMF), KH-induced reconnection is not limited to specific regions around the vortices (inside,  
521 below or above). It is rather triggered over a broad and continuous range of locations near the vortices,  
522 so that the distinction between mid-latitude and type I (Vortex-induced) reconnection is harder to make,  
523 if at all meaningful, as also suggested in a recent simulation of this event by *Sisti et al.* [2019]).

524

## 525 **5 Conclusions**

526 We studied the properties of Kelvin-Helmholtz induced magnetic reconnection by means of 3D MHD and  
527 two-fluid simulations and data analysis from the MMS mission. The global simulation demonstrates that  
528 the location of the most unstable KH region at the Earth's magnetopause is not confined to the  
529 equatorial plane, but rather distributed over a range of latitude, and shifted to the northern or southern  
530 hemisphere, depending on the upstream IMF clock angle. The two-fluid simulation particularly confirms  
531 this point, as also shown in *Fadanelli et al.* [2018], with a clear shift of the vortices location.

532 We then investigated magnetic reconnection on a local scale within the KH vortices, and in particular on  
533 the trailing edge of the waves. Owing to the typical large-scale configuration at the magnetospheric  
534 flanks where the KH instability develops, magnetic reconnection induced by KH waves has a strong guide  
535 field component. This is of particular interest to study the onset properties of magnetic reconnection  
536 under such conditions. We tested the model proposed by *Swisdak et al.* [2003] and found that all  
537 observed events fulfilled the condition for reconnection to occur, including those without reconnection  
538 signatures. This shows that the diamagnetic suppression condition works also in that regime, but the fact  
539 that all non-reconnecting events are found in "possibly" reconnecting conditions confirms that this  
540 model provides a necessary but not sufficient condition for reconnection to occur.

541 In addition, thanks to the high quality of the MMS data, we were able to derive several variants of the  
542 suppression condition for each observed event. The most accurate variant makes use of the full pressure  
543 tensor and was not used in previous studies based on different datasets. We show in our study that the  
544 use of a simplified model can lead to a significant under-estimation of the range of conditions that are  
545 favorable for reconnection.

546 Finally, by combining simulations and data analysis we found that the reconnecting current sheets  
547 observed by MMS are broadly distributed ( $20^\circ$ ) and all southward of the most unstable region at the  
548 magnetopause. This finding is consistent with recent simulations by *Fadanelli et al.* [2018] and *Sisti et al.*  
549 [2019] suggesting that magnetic reconnection occurs over a broad range of latitudes, and so that vortex-  
550 induced (type I) and mid-latitude reconnection are hard to separate when a significant magnetic shear  
551 exists at the flank magnetopause (i.e., non-purely northward IMF).

552

## 553 **APPENDIX A: Magnetopause detection procedure in the global MHD simulation code BATS'R'US**

554 In order to derive properly the growth rate at the Earth's magnetopause, we need to find the  
555 magnetopause position in the simulation run. Our method is as follows. (1) We initialize a magnetopause  
556 surface using the *Shue et al.* [1997] model and the upstream parameters of the simulation. The modeled

557 distance is systematically larger than that in the global MHD run. For each point at the magnetopause,  
 558 we search for the maximum current density, using a Gaussian fit, along the normal to the magnetopause  
 559 as estimated from the *Shue et al. [1997]* model. We illustrate this magnetopause detection scheme in  
 560 Figure 7, which shows the current density and the  $X_{\text{GSM}}$  component of the velocity in the meridional  
 561 plane, the equatorial plane, and on a plane at  $45^\circ$  between the two previous planes. The scatter points  
 562 show our magnetopause detection as well as the points in the magnetosphere and magnetosheath used  
 563 to derive the Kelvin-Helmholtz instability growth rate.

564

565 **APPENDIX B:** Local simulation of the KH vortices at the magnetopause.

566 In a simplified slab geometry, we assume  $\hat{x}$  to be perpendicular to the unperturbed magnetopause,  $\hat{y}$   
 567 along the flow and  $\hat{z}$  represents the latitude direction. We start from a slab MHD equilibrium, depending  
 568 on  $x$  and  $z$  only, that mimics the gradual stabilization of the KH instability away from  $z = 0$  where the  
 569 growth rate is maximal. In this equilibrium, all physical quantities but the  $x$  and  $z$ -component of the  
 570 magnetic field are functions of the flow-aligned component  $\Psi$  of the equilibrium vector potential  
 571 [*Andreussi et al., 2012*] while  $B_{x,eq}$  and  $B_{z,eq}$  are simply given by the rotational of  $\psi\hat{y}$ .

572 We set  $\psi(x, z) = B_{z,av}[4/3x + L_z/3\pi \sinh(2\pi x/L_z)\cos(2\pi z/L_z)]/2$  and  $B_{y,eq} = B_{flow}(1 +$   
 573  $\tanh(\Psi/a))$ , where  $a$  is the half-width of the unperturbed magnetopause,  $B_{z,av}$  the averaged northward  
 574 field and  $B_{flow}$  the flow-aligned component of the IMF (all quantities are normalized to the ion skip  
 575 depth  $d_i$ , the ion cyclotron frequency  $\Omega_{ci}$  and the ion mass  $m_i$ . Taking  $x \in [-L_x/2, +L_x/2]$  and  $a \ll$   
 576  $L_x \ll L_z$  we obtain a magnetic field that is nearly northward inside the magnetosphere and that has a  
 577 flow aligned component  $B_{flow}$  outside it.

578 The high-latitude stabilization is achieved assuming  $U_{eq} = \Delta U/2 \tanh(\psi/a)\hat{y}$ . Indeed the velocity  
 579 gradient at the magnetopause ( $x = 0$ ) is three times bigger at  $z = 0$  than its value at the  $z$ -boundaries at  
 580  $z = \pm L_z/2$ . Consequently, the KH instability grows much faster around  $z = 0$  than at high latitudes  
 581 [*Faganello et al., 2012a*] that remain nearly unperturbed during the development of the instability at low  
 582 latitude.

583 The plasma density is given by  $n_{eq} = n_{av} + |n_{sh} - n_{sp}|/2 \tanh(\psi/a)$ , where  $n_{sh}$ ,  $n_{sp}$ , and  $n_{av}$  are the  
 584 magnetosheath, the magnetosphere and the average density, respectively. The thermal pressure  
 585 assures  $P_{th,eq} + B_{flow}^2/2 = \Pi = cst$ , so that the Grad-Shafranov equation (force-balance equation in  
 586 field-aligned coordinates)  $\nabla^2\psi = \partial_\psi\Pi$  is satisfied. We set the ratio between the ion and electron  
 587 temperatures equal to four. All the plasma quantities are taken as close as possible to those measured  
 588 by MMS satellites across the magnetopause and are resumed in Table 1.

589 The system evolution is described by Hall-MHD equations that include the electron diamagnetic term  
 590 and a small but finite resistivity ( $\eta = 10^{-3}$  in adimensional units) in the generalized Ohm's law. We  
 591 consider adiabatic closures for both ions and electrons. All equations are advanced in time by a 4th-order  
 592 Runge-Kutta scheme. Spatial derivatives are performed via 6th-order finite differences along the periodic  
 593  $y$  and  $z$  directions, while using a 4th-order compact implicit scheme [*Lele, 1992*] for the more critical  
 594 open  $x$ -direction. At the  $x$ -boundaries, we adopt a decomposition on MHD characteristic that lets all  
 595 MHD perturbations simply leave the domain [*Landi et al., 2005; Faganello et al., 2009*].



596 We set the magnetopause half-width  $a = 3$ , consequently the wavelength (along  $\hat{y}$ ) of the more unstable  
597 KH mode is  $\lambda_{KH} \approx 12\pi$ . Taking an “effective” ion skin depth  $d_i \approx 300 \text{ km}$  we obtain a physical  
598 wavelength  $\approx 12000 \text{ km}$  (in practice the importance of the Hall term is slightly enhanced in our  
599 simulation but we are able to correctly resolve it).

600 The box dimensions are  $L_x = 60$ ,  $L_y = 24\pi$ , and  $L_z = 120\pi$ , so that the KH instability develops two  
601 vortices along  $\hat{y}$ . The number of points in each direction is  $n_x = 600$ ,  $n_y = 512$ ,  $n_z = 512$ .  $L_z$  was  
602 chosen from the outcome of the global simulation. It is compatible with the global simulations and  
603 allows for a sufficient instability, compared to KH vortex size, so as to allow vortex pairing in the non-  
604 linear stage. The unstable zone needs to be sufficiently thick, as shown in *Takagi et al.* [2006].

605 Finally, the density on the magnetospheric side is  $n = 6.5 \text{ cm}^{-3}$ , and the plasma  $\beta = 1.82$ , while on the  
606 magnetosheath side these parameters are  $n = 19.5 \text{ cm}^{-3}$  and  $\beta = 1.58$ , consistent with MMS observations.

607

## 608 Acknowledgments

609 Simulation results have been provided by the Community Coordinated Modeling Center at Goddard  
610 Space Flight Center through their public Runs on Request system (<http://ccmc.gsfc.nasa.gov>). The BATS-  
611 R-US Model was developed by Dr. Tamas Gombosi at the University of Michigan. The run is stored at:  
612 [https://ccmc.gsfc.nasa.gov/results/viewrun.php?domain=GM&runnumber=Yoann\\_Vernisse\\_012518\\_1](https://ccmc.gsfc.nasa.gov/results/viewrun.php?domain=GM&runnumber=Yoann_Vernisse_012518_1).  
613 The two-fluid simulation data are stored in the PIIM laboratory repository and are available at  
614 <https://storagepiim.etoile.univ-amu.fr/share.cgi?ssid=00SbRzp>. For MMS data visit  
615 <https://lasp.colorado.edu/mms/sdc/public/>. We thank all the MMS teams for their remarkable work and  
616 great hardware accomplishments. IRAP contribution to MMS was performed with the support of CNRS  
617 and CNES. FC has received funding from the European Union’s Horizon 2020 research and innovation  
618 programme under grant agreement No 776262 (AIDA).

619

## 620 Bibliography

621 Andreussi, T., Morrison, P. J., & Pegoraro, F. (2012). Hamiltonian magnetohydrodynamics: Helically  
622 symmetric formulation, Casimir invariants, and equilibrium variational principles. *Physics of*  
623 *Plasmas*, 19, 052102. <https://doi.org/10.1063/1.4714761>

624 Borgogno, D., Califano, F., Faganello, M., & Pegoraro, F. (2015). Double-reconnected magnetic  
625 structures driven by Kelvin-Helmholtz vortices at the Earth’s magnetosphere. *Physics of*  
626 *Plasmas*, 22(3), 032301. <https://doi.org/10.1063/1.4913578>

627 Burch, J. L., Moore, T. E., Torbert, R. B., & Giles, B. L. (2015). Magnetospheric Multiscale Overview  
628 and Science Objectives. *Space Science Reviews*. <https://doi.org/10.1007/s11214-015-0164-9>

62Burch, J. L., Torbert, R. B., Phan, T. D., Chen, L.-J., Moore, T. E., Ergun, R. E., ... Chandler, M.  
630 (2016). Electron-scale measurements of magnetic reconnection in space. *Science*.  
631 <https://doi.org/10.1126/science.aaf2939>

632Chandrasekhar, S. (1961). *Hydrodynamic and hydromagnetic stability*. Consulté à l'adresse  
633 <http://cdsads.u-strasbg.fr/abs/1961hhs..book.....C>

634Chen, Q., Otto, A., & Lee, L. C. (1997). Tearing instability, Kelvin-Helmholtz instability, and  
635 magnetic reconnection. *Journal of Geophysical Research*, *102*, 151-162.  
636 <https://doi.org/10.1029/96JA03144>

637Eriksson, S., Lavraud, B., Wilder, F. D., Stawarz, J. E., Giles, B. L., Burch, J. L., ... Goodrich, K. A.  
638 (2016). Magnetospheric Multiscale observations of magnetic reconnection associated with  
639 Kelvin-Helmholtz waves. *Geophysical Research Letters*, *43*, 5606-5615.  
640 <https://doi.org/10.1002/2016GL068783>

641Fadanelli, S., Faganello, M., Califano, F., Cerri, S. S., Pegoraro, F., & Lavraud, B. (2018). North-  
642 South asymmetric Kelvin-Helmholtz instability and induced reconnection at the Earth's  
643 magnetospheric flanks. *ArXiv e-prints*, *1805*, arXiv:1805.01466.

644Faganello, M., Califano, F., & Pegoraro, F. (2008). Time Window for Magnetic Reconnection in  
645 Plasma Configurations with Velocity Shear. *Physical Review Letters*, *101*, 175003.  
646 <https://doi.org/10.1103/PhysRevLett.101.175003>

647Faganello, M., Califano, F., & Pegoraro, F. (2009). Being on time in magnetic reconnection. *New*  
648 *Journal of Physics*, *11*, 063008. <https://doi.org/10.1088/1367-2630/11/6/063008>

649Faganello, M., Califano, F., Pegoraro, F., & Andreussi, T. (2012a). Double mid-latitude dynamical  
650 reconnection at the magnetopause: An efficient mechanism allowing solar wind to enter the  
651 Earth's magnetosphere. *EPL (Europhysics Letters)*, *100*, 69001. [https://doi.org/10.1209/0295-  
652 5075/100/69001](https://doi.org/10.1209/0295-5075/100/69001)

653 Faganello, M., Califano, F., Pegoraro, F., Andreussi, T., & Benkadda, S. (2012b). Magnetic  
654 reconnection and Kelvin-Helmholtz instabilities at the Earth's magnetopause. *Plasma Physics  
655 and Controlled Fusion*, 54(12), 124037. <https://doi.org/10.1088/0741-3335/54/12/124037>

656 Faganello, M., Califano, F., Pegoraro, F., & Retinò, A. (2014). Kelvin-Helmholtz vortices and double  
657 mid-latitude reconnection at the Earth's magnetopause: Comparison between observations and  
658 simulations. *EPL (Europhysics Letters)*, 107, 19001. [https://doi.org/10.1209/0295-  
659 5075/107/19001](https://doi.org/10.1209/0295-5075/107/19001)

660 Faganello, Matteo, & Califano, F. (2017). Magnetized Kelvin-Helmholtz instability: theory and  
661 simulations in the Earth's magnetosphere context. *Journal of Plasma Physics*, 83, 535830601.  
662 <https://doi.org/10.1017/S0022377817000770>

663 Fairfield, D. H., Otto, A., Mukai, T., Kokubun, S., Lepping, R. P., Steinberg, J. T., ... Yamamoto, T.  
664 (2000). Geotail observations of the Kelvin-Helmholtz instability at the equatorial magnetotail  
665 boundary for parallel northward fields. *Journal of Geophysical Research*, 105, 21.  
666 <https://doi.org/10.1029/1999JA000316>

667 Farrugia, C. J., Gratton, F. T., Bender, L., Biernat, H. K., Erkaev, N. V., Quinn, J. M., ... Dennisenko,  
668 V. (1998). Charts of joint Kelvin-Helmholtz and Rayleigh-Taylor instabilities at the dayside  
669 magnetopause for strongly northward interplanetary magnetic field. *Journal of Geophysical  
670 Research*, 103, 6703-6728. <https://doi.org/10.1029/97JA03248>

671 Foullon, C., Farrugia, C. J., Owen, C. J., Fazakerley, A. N., & Gratton, F. T. (2010). Kelvin-Helmholtz  
672 Multi-Spacecraft Studies at the Earth's Magnetopause Boundaries. *Twelfth International Solar  
673 Wind Conference*, 1216, 483-486. <https://doi.org/10.1063/1.3395908>

674 Frank, A., Jones, T. W., Ryu, D., & Gaalaas, J. B. (1996). The Magnetohydrodynamic Kelvin-  
675 Helmholtz Instability: A Two-dimensional Numerical Study. *The Astrophysical Journal*, 460,  
676 777. <https://doi.org/10.1086/177009>

677 Fuselier, S. A., Anderson, B. J., & Onsager, T. G. (1995). Particle signatures of magnetic topology at  
678 the magnetopause: AMPTE/CCE observations. *Journal of Geophysical Research*, *100*, 11.  
679 <https://doi.org/10.1029/94JA02811>

680 Fuselier, S. A., Anderson, B. J., & Onsager, T. G. (1997). Electron and ion signatures of field line  
681 topology at the low-shear magnetopause. *Journal of Geophysical Research*, *102*, 4847-4864.  
682 <https://doi.org/10.1029/96JA03635>

683 Fuselier, S. A., Vines, S. K., Burch, J. L., Petrinec, S. M., Trattner, K. J., Cassak, P. A., ... Webster, J.  
684 M. (2017). Large-scale characteristics of reconnection diffusion regions and associated  
685 magnetopause crossings observed by MMS. *Journal of Geophysical Research (Space Physics)*,  
686 *122*, 5466-5486. <https://doi.org/10.1002/2017JA024024>

687 Gosling, J. T., & Phan, T. D. (2013). Magnetic Reconnection in the Solar Wind at Current Sheets  
688 Associated with Extremely Small Field Shear Angles. *The Astrophysical Journal Letters*, *763*,  
689 L39. <https://doi.org/10.1088/2041-8205/763/2/L39>

690 Harvey, C. C. (1998). Spatial Gradients and the Volumetric Tensor. *ISSI Scientific Reports Series*, *1*,  
691 307-322.

692 Hasegawa, H., Fujimoto, M., Phan, T.-D., Rème, H., Balogh, A., Dunlop, M. W., ... TanDokoro, R.  
693 (2004). Transport of solar wind into Earth's magnetosphere through rolled-up Kelvin-Helmholtz  
694 vortices. *Nature*, *430*, 755-758. <https://doi.org/10.1038/nature02799>

695 Hesse, M., Aunai, N., Birn, J., Cassak, P., Denton, R. E., Drake, J. F., ... Zenitani, S. (2016). Theory  
696 and Modeling for the Magnetospheric Multiscale Mission. *Space Science Reviews*, *199*, 577-630.  
697 <https://doi.org/10.1007/s11214-014-0078-y>

698 Kavosi, S., & Raeder, J. (2015). Ubiquity of Kelvin-Helmholtz waves at Earth's magnetopause.  
699 *Nature Communications*, *6*, 7019. <https://doi.org/10.1038/ncomms8019>

700 King, J. H., & Papitashvili, N. E. (2005). Solar wind spatial scales in and comparisons of hourly Wind  
701 and ACE plasma and magnetic field data. *Journal of Geophysical Research: Space Physics*,  
702 110(A2), n/a–n/a. <https://doi.org/10.1029/2004JA010649>

703 Knoll, D. A., & Chacón, L. (2002). Magnetic Reconnection in the Two-Dimensional Kelvin-  
704 Helmholtz Instability. *Physical Review Letters*, 88, 215003.  
705 <https://doi.org/10.1103/PhysRevLett.88.215003>

706 Kobayashi, S., Rogers, B. N., & Numata, R. (2014). Gyrokinetic simulations of collisionless  
707 reconnection in turbulent non-uniform plasmas. *Physics of Plasmas*, 21, 040704.  
708 <https://doi.org/10.1063/1.4873703>

709 Landi, S., Velli, M., & Einaudi, G. (2005). Alfvén Waves and Shock Wave Formation at an X-Point  
710 Magnetic Field Configuration. *The Astrophysical Journal*, 624, 392-401.  
711 <https://doi.org/10.1086/428822>

712 Lavraud, B., Thomsen, M. F., Lefebvre, B., Schwartz, S. J., Seki, K., Phan, T. D., ... Balogh, A.  
713 (2006). Evidence for newly closed magnetosheath field lines at the dayside magnetopause under  
714 northward IMF. *Journal of Geophysical Research (Space Physics)*, 111, A05211.  
715 <https://doi.org/10.1029/2005JA011266>

716 Lavraud, B., Thomsen, M. F., Taylor, M. G. G. T., Wang, Y. L., Phan, T. D., Schwartz, S. J., ...  
717 Balogh, A. (2005). Characteristics of the magnetosheath electron boundary layer under northward  
718 interplanetary magnetic field: Implications for high-latitude reconnection. *Journal of Geophysical*  
719 *Research (Space Physics)*, 110, A06209. <https://doi.org/10.1029/2004JA010808>

720 Dele, S. K. (1992). Compact Finite Difference Schemes with Spectral-like Resolution. *Journal of*  
721 *Computational Physics*, 103, 16-42. [https://doi.org/10.1016/0021-9991\(92\)90324-R](https://doi.org/10.1016/0021-9991(92)90324-R)

722 Li, W., André, M., Khotyaintsev, Y. V., Vaivads, A., Graham, D. B., Toledo-Redondo, S., ...  
723 Strangeway, R. J. (2016). Kinetic evidence of magnetic reconnection due to Kelvin-Helmholtz  
724 waves. *Geophysical Research Letters*, n/a–n/a. <https://doi.org/10.1002/2016GL069192>

725 Lin, D., Wang, C., Li, W., Tang, B., Guo, X., & Peng, Z. (2014). Properties of Kelvin-Helmholtz  
726 waves at the magnetopause under northward interplanetary magnetic field: Statistical study.  
727 *Journal of Geophysical Research (Space Physics)*, 119, 7485-7494.  
728 <https://doi.org/10.1002/2014JA020379>

729 Liu, Y.-H., & Hesse, M. (2016). Suppression of collisionless magnetic reconnection in asymmetric  
730 current sheets. *Physics of Plasmas*, 23, 060704. <https://doi.org/10.1063/1.4954818>

731 Liu, Z. X., & Hu, Y. D. (1988). Local magnetic reconnection caused by vortices in the flow field.  
732 *Geophysical Research Letters*, 15, 752-755. <https://doi.org/10.1029/GL015i008p00752>

733 Ma, X., Delamere, P., Otto, A., & Burkholder, B. (2017). Plasma Transport Driven by the Three-  
734 Dimensional Kelvin-Helmholtz Instability. *Journal of Geophysical Research: Space Physics*,  
735 122(10), 2017JA024394. <https://doi.org/10.1002/2017JA024394>

736 Masters, A. (2014). Magnetic reconnection at Uranus' magnetopause. *Journal of Geophysical*  
737 *Research (Space Physics)*, 119, 5520-5538. <https://doi.org/10.1002/2014JA020077>

738 Masters, A. (2015). Magnetic reconnection at Neptune's magnetopause. *Journal of Geophysical*  
739 *Research (Space Physics)*, 120, 479-493. <https://doi.org/10.1002/2014JA020744>

740 Masters, A., Eastwood, J. P., Swisdak, M., Thomsen, M. F., Russell, C. T., Sergis, N., ... Krimigis, S.  
741 M. (2012). The importance of plasma  $\beta$  conditions for magnetic reconnection at Saturn's  
742 magnetopause. *Geophysical Research Letters*, 39, L08103.  
743 <https://doi.org/10.1029/2012GL051372>

744 McNally, C. P., Lyra, W., & Passy, J.-C. (2012). A Well-posed Kelvin-Helmholtz Instability Test and  
745 Comparison. *The Astrophysical Journal Supplement Series*, 201, 18.  
746 <https://doi.org/10.1088/0067-0049/201/2/18>

747 Miura, A., & Pritchett, P. L. (1982). Nonlocal stability analysis of the MHD Kelvin-Helmholtz  
748 instability in a compressible plasma. *Journal of Geophysical Research*, 87, 7431-7444.  
749 <https://doi.org/10.1029/JA087iA09p07431>

750 Miura, Akira. (1995). Dependence of the magnetopause Kelvin-Helmholtz instability on the  
751 orientation of the magnetosheath magnetic field. *Geophysical Research Letters*, 22, 2993-2996.  
752 <https://doi.org/10.1029/95GL02793>

753 Nakamura, T. K. M., & Fujimoto, M. (2005). Magnetic reconnection within rolled-up MHD-scale  
754 Kelvin-Helmholtz vortices: Two-fluid simulations including finite electron inertial effects.  
755 *Geophysical Research Letters*, 32, L21102. <https://doi.org/10.1029/2005GL023362>

756 Nakamura, T. K. M., Fujimoto, M., & Otto, A. (2008). Structure of an MHD-scale Kelvin-Helmholtz  
757 vortex: Two-dimensional two-fluid simulations including finite electron inertial effects. *Journal*  
758 *of Geophysical Research (Space Physics)*, 113, A09204. <https://doi.org/10.1029/2007JA012803>

759 Nakamura, T. K. M., Hasegawa, H., Shinohara, I., & Fujimoto, M. (2011). Evolution of an MHD-  
760 scale Kelvin-Helmholtz vortex accompanied by magnetic reconnection: Two-dimensional  
761 particle simulations. *Journal of Geophysical Research (Space Physics)*, 116, A03227.  
762 <https://doi.org/10.1029/2010JA016046>

763 Nakamura, T. K. M., Daughton, W., Karimabadi, H., & Eriksson, S. (2013). Three-dimensional  
764 dynamics of vortex-induced reconnection and comparison with THEMIS observations. *Journal of*  
765 *Geophysical Research: Space Physics*, 118, 5742– 5757. <https://doi.org/10.1002/jgra.50547>

766 Nakamura, T. K. M., Eriksson, S., Hasegawa, H., Zenitani, S., Li, W. Y., Genestreti, K. J., ...  
767 Daughton, W. (2017a), Mass and energy transfer across the Earth's magnetopause caused by

768 vortex-induced reconnection. *Journal of Geophysical Research: Space Physics*, 2017JA024346.

769 <https://doi.org/10.1002/2017JA024346>

770 Nakamura, T. K. M., Hasegawa, H., Daughton, W., Eriksson, S., Li, W. Y., & Nakamura, R. (2017b).

771 Turbulent mass transfer caused by vortex induced reconnection in collisionless magnetospheric

772 plasmas. *Nature Communications*, 8, 1582. <https://doi.org/10.1038/s41467-017-01579-0>

773 Nykyri, K., Otto, A., Lavraud, B., Mouikis, C., Kistler, L. M., Balogh, A., & Rème, H. (2006). Cluster

774 observations of reconnection due to the Kelvin-Helmholtz instability at the dawnside

775 magnetospheric flank. *Annales Geophysicae*, 24, 2619-2643. [https://doi.org/10.5194/angeo-24-](https://doi.org/10.5194/angeo-24-2619-2006)

776 [2619-2006](https://doi.org/10.5194/angeo-24-2619-2006)

777 Nykyri, Katariina, Ma, X., Dimmock, A., Foullon, C., Otto, A., & Osmane, A. (2017). Influence of

778 velocity fluctuations on the Kelvin-Helmholtz instability and its associated mass transport.

779 *Journal of Geophysical Research (Space Physics)*, 122, 9489-9512.

780 <https://doi.org/10.1002/2017JA024374>

781 Onsager, T. G., Scudder, J. D., Lockwood, M., & Russell, C. T. (2001). Reconnection at the high-

782 latitude magnetopause during northward interplanetary magnetic field conditions. *Journal of*

783 *Geophysical Research*, 106, 25467-25488. <https://doi.org/10.1029/2000JA000444>

784 Otto, A., & Fairfield, D. H. (2000). Kelvin-Helmholtz instability at the magnetotail boundary: MHD

785 simulation and comparison with Geotail observations. *Journal of Geophysical Research*, 105, 21.

786 <https://doi.org/10.1029/1999JA000312>

787 Phan, T. D., Gosling, J. T., Paschmann, G., Pasma, C., Drake, J. F., Øieroset, M., ... Davis, M. S.

788 (2010). The Dependence of Magnetic Reconnection on Plasma  $\beta$  and Magnetic Shear: Evidence

789 from Solar Wind Observations. *The Astrophysical Journal Letters*, 719, L199-L203.

790 <https://doi.org/10.1088/2041-8205/719/2/L199>



79Phan, T. D., Love, T. E., Gosling, J. T., Paschmann, G., Eastwood, J. P., Oieroset, M., ... Auster, U.

792 (2011). Triggering of magnetic reconnection in a magnetosheath current sheet due to

793 compression against the magnetopause. *Geophysical Research Letters*, 38, L17101.

794 <https://doi.org/10.1029/2011GL048586>

79Phan, T. D., Paschmann, G., Gosling, J. T., Oieroset, M., Fujimoto, M., Drake, J. F., & Angelopoulos,

796 V. (2013). The dependence of magnetic reconnection on plasma  $\beta$  and magnetic shear: Evidence

797 from magnetopause observations. *Geophysical Research Letters*, 40, 11-16.

798 <https://doi.org/10.1029/2012GL054528>

79Phan, T., Dunlop, M., Paschmann, G., Klecker, B., Bosqued, J., Rème, H., ... Kistler, L. (2004a).

800 Cluster observations of continuous reconnection at the magnetopause under steady interplanetary

801 magnetic field conditions. *Annales Geophysicae*, 22, 2355-2367. <https://doi.org/10.5194/angeo->

802 [22-2355-2004](https://doi.org/10.5194/angeo-22-2355-2004)

80Phan, T., Dunlop, M., Paschmann, G., Klecker, B., Bosqued, J., Rème, H., ... Kistler, L. (2004b).

804 Cluster observations of continuous reconnection at the magnetopause under steady interplanetary

805 magnetic field conditions. *Annales Geophysicae*, 22, 2355-2367. <https://doi.org/10.5194/angeo->

806 [22-2355-2004](https://doi.org/10.5194/angeo-22-2355-2004)

80Powell, K. G., Roe, P. L., Linde, T. J., Gombosi, T. I., & De Zeeuw, D. L. (1999). A Solution-

808 Adaptive Upwind Scheme for Ideal Magnetohydrodynamics. *Journal of Computational Physics*,

809 154, 284-309. <https://doi.org/10.1006/jcph.1999.6299>

81Priest, E., & Forbes, T. (2000). Unsteady Reconnection: The Tearing Mode. In *Magnetic*

811 *reconnection : MHD theory and applications* (p. 177-204). Cambridge University Press.

81 Raeder, J., Larson, D., Li, W., Kepko, E. L., & Fuller-Rowell, T. (2008). OpenGGCM Simulations for  
813 the THEMIS Mission. *Space Science Reviews*, *141*, 535-555. [https://doi.org/10.1007/s11214-](https://doi.org/10.1007/s11214-008-9421-5)  
814 [008-9421-5](https://doi.org/10.1007/s11214-008-9421-5)

815 Shue, J.-H., Chao, J. K., Fu, H. C., Russell, C. T., Song, P., Khurana, K. K., & Singer, H. J. (1997). A  
816 new functional form to study the solar wind control of the magnetopause size and shape. *Journal*  
817 *of Geophysical Research*, *102*, 9497-9512. <https://doi.org/10.1029/97JA00196>

818 Sonnerup, B. U. Ö., & Scheible, M. (1998). Minimum and Maximum Variance Analysis. *ISSI*  
819 *Scientific Reports Series*, *1*, 185-220.

820 Stawarz, J. E., Eriksson, S., Wilder, F. D., Ergun, R. E., Schwartz, S. J., Pouquet, A., ... Sturmer, A. P.  
821 (2016). Observations of turbulence in a Kelvin-Helmholtz event on 8 September 2015 by the  
822 Magnetospheric Multiscale mission. *Journal of Geophysical Research (Space Physics)*, *121*, 11.  
823 <https://doi.org/10.1002/2016JA023458>

824 Swisdak, M., Opher, M., Drake, J. F., & Alouani Bibi, F. (2010). The Vector Direction of the  
825 Interstellar Magnetic Field Outside the Heliosphere. *The Astrophysical Journal*, *710*, 1769-1775.  
826 <https://doi.org/10.1088/0004-637X/710/2/1769>

827 Swisdak, M., Rogers, B. N., Drake, J. F., & Shay, M. A. (2003). Diamagnetic suppression of  
828 component magnetic reconnection at the magnetopause. *Journal of Geophysical Research (Space*  
829 *Physics)*, *108*, 1218. <https://doi.org/10.1029/2002JA009726>

830 Takagi, K., Hashimoto, C., Hasegawa, H., Fujimoto, M., and TanDokoro, R. (2006), Kelvin-  
831 Helmholtz instability in a magnetotail flank-like geometry: Three-dimensional MHD simulations,  
832 *J. Geophys. Res.*, *111*, A08202, doi:10.1029/2006JA011631.

833 Vernisse, Y., Lavraud, B., Eriksson, S., Gershman, D. J., Dorelli, J., Pollock, C., ... Yokota, S. (2016).  
834 Signatures of complex magnetic topologies from multiple reconnection sites induced by Kelvin-

835 Helmholtz instability. *Journal of Geophysical Research: Space Physics*, 121(10), 9926–9939.

836 <https://doi.org/10.1002/2016JA023051>

837 Wilber, M., & Winglee, R. M. (1995). Dawn-dusk asymmetries in the low-latitude boundary layer

838 arising from the Kelvin-Helmholtz instability: A particle simulation. *Journal of Geophysical*

839 *Research*, 100, 1883-1898. <https://doi.org/10.1029/94JA02488>

840

841

842

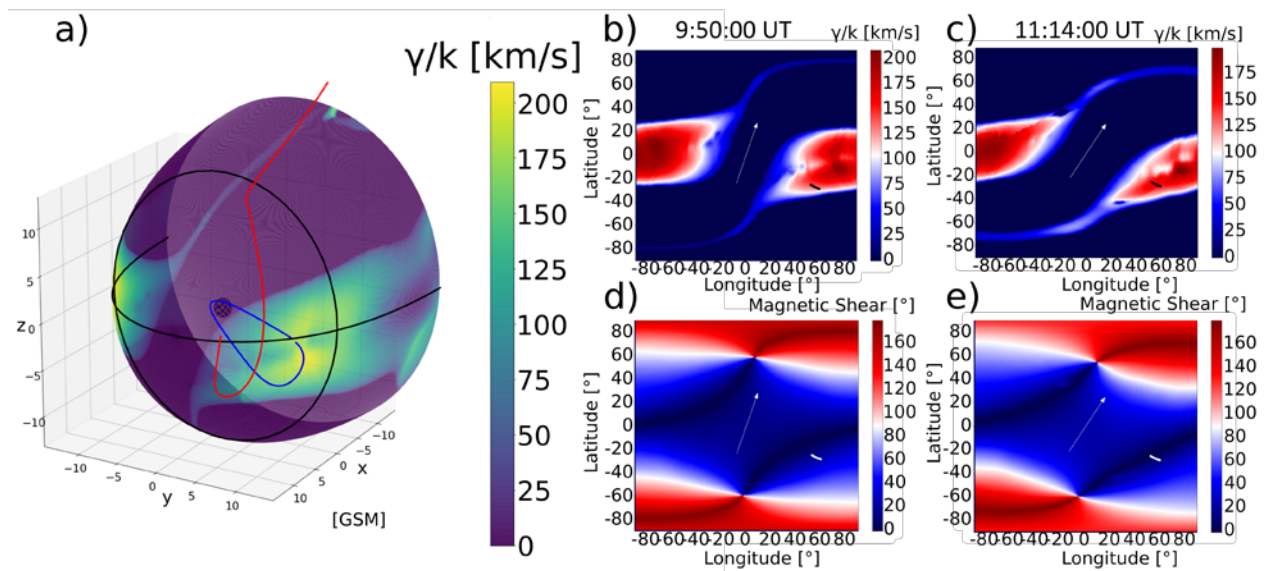
	$B_{z,av}$	$B_{flow}$	$\Delta U$	$n_{av}$	$\Delta n$	$T_{av}$	$\Delta T$
Normalized	1	-0.3	0.9	1	1	15/16	$\sim -1.3$
physical	67 nT	-20 nT	360 km/s	13 cm <sup>-3</sup>	13 cm <sup>-3</sup>	1500 eV	2080 eV

843

844 **Table 1:** Equilibrium quantities expressed in normalized and physical units. We recall that the subscript

845 “av” denotes the averaged values that these quantities have at the magnetopause.

846



847

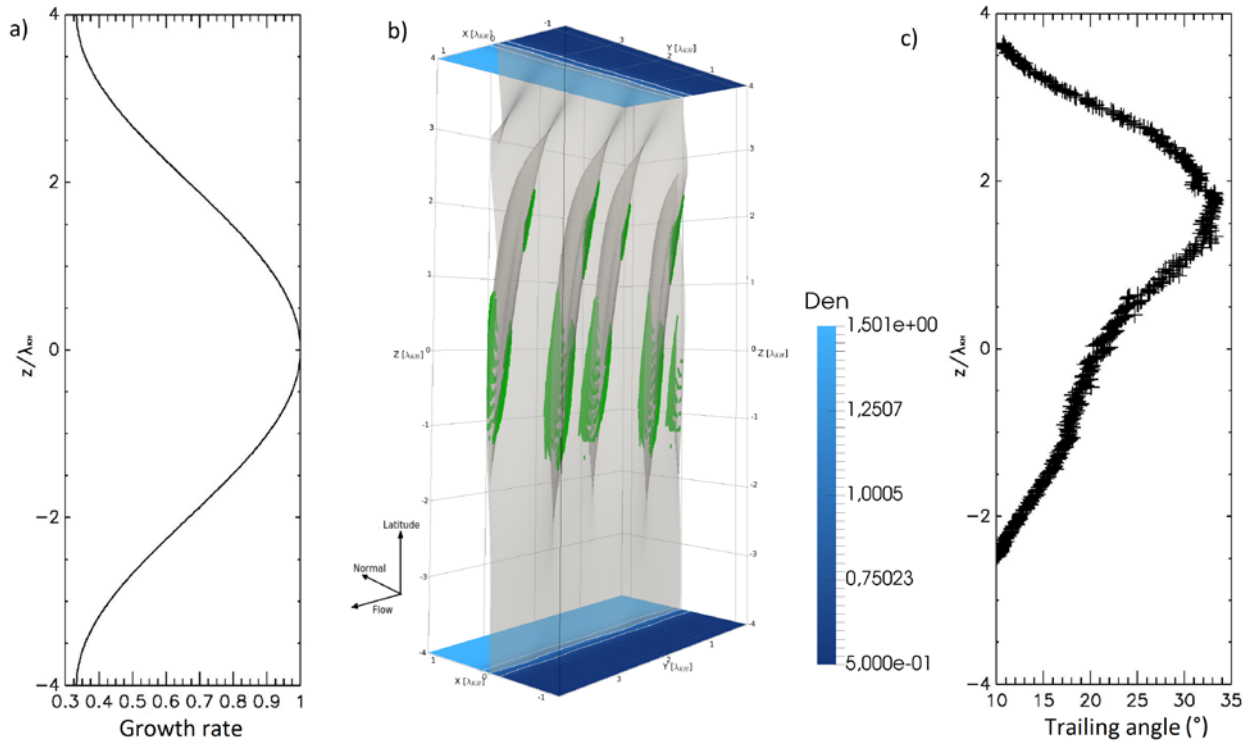
848 **Figure 1:**

849 Results from the three-dimensional MHD simulation code Bats'R'us in the GSM coordinate system.

850 Inputs of the simulation are provided by the OMNI data. Panel a: three-dimensional representation of

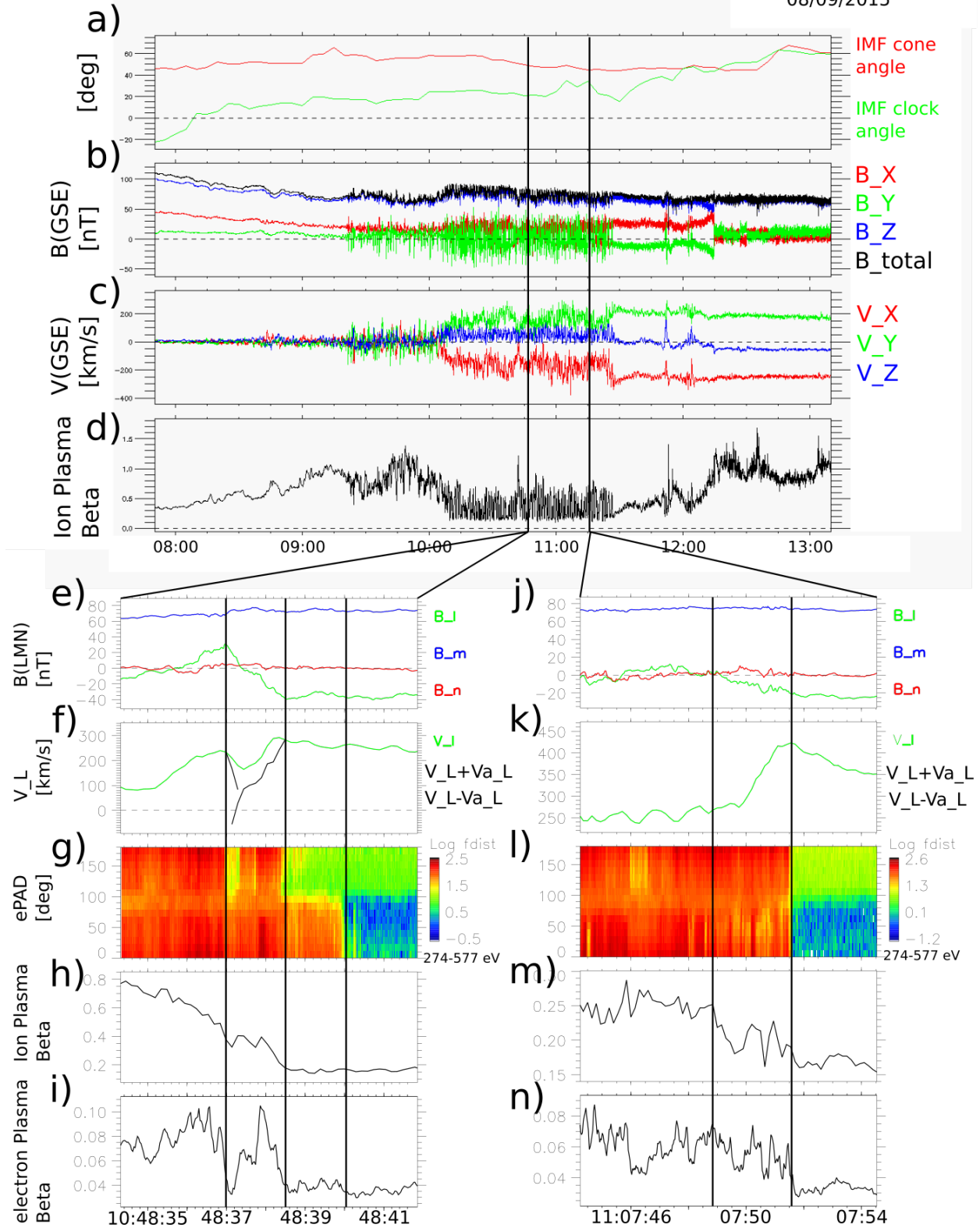
851 the growth rate calculated at the magnetopause. The terminator (black), the equatorial plane (black), the

852 orbit of the MMS spacecraft (blue), and a magnetic field line (red) are plotted(see text for detail). Panels  
 853 b and c represent the growth rate at the magnetopause at 9:50:00 UT and 11:14:00 UT, respectively,  
 854 while Panels d and e present the magnetic shear angle at the magnetopause at the same time. The IMF  
 855 clock angle is represented by a white arrow in panels b to e. The positions of the MMS spacecraft from  
 856 8:30 UT to 11:30 UT are represented by black dots in panels b and c, and white dots in panels d and e.



857  
 858 **Figure 2:**  
 859 Results from the local two-fluid simulation. a) normalized KH growth rate as a function of  $z$ . b) a 3D  
 860 rendering of the simulation results at the beginning of the non-linear phase ( $t\omega_{ci} = 525$ ). Blue and light  
 861 blue colors represent the plasma density. White lines in the upper and lower planes are drawn at  
 862 normalized plasma density = 0.7, 1.0, 1.3. The shaded surface represents the magnetopause folded by  
 863 the vortices. Regions where the component of the magnetic field perpendicular to the folded  
 864 magnetopause has a magnitude larger than 2% of the magnetospheric field are drawn in green. c) the  
 865 trailing angle as a function of  $z$  at  $t\omega_{ci} = 525$ .  
 866

08/09/2015

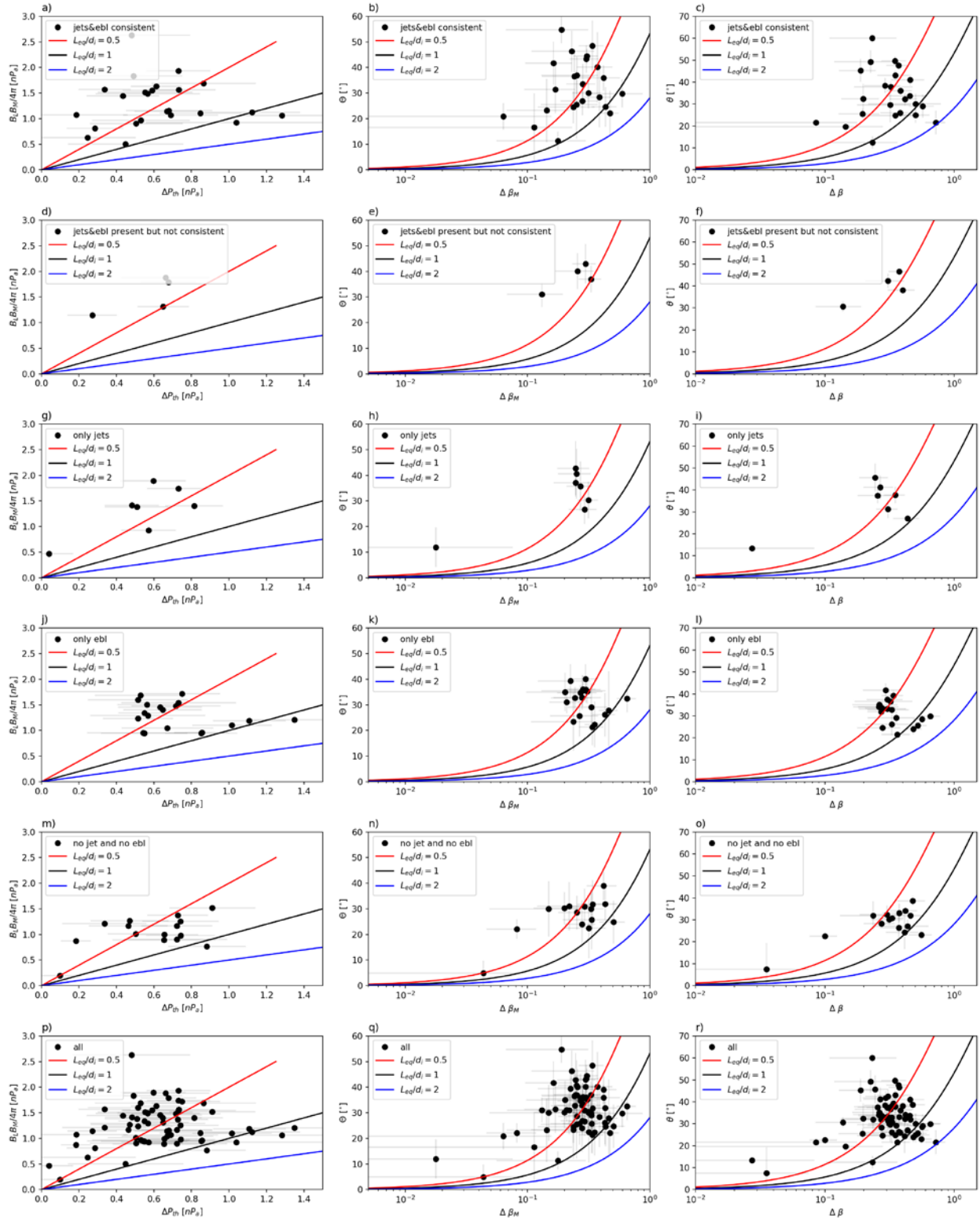


867  
868

Figure 3:

869 Panel a): IMF cone angle and clock angle (in GSM) derived from OMNI data. Panels b), c), and d):  
870 Magnetic field, velocity, and ion plasma beta from the MMS1 spacecraft (GSE coordinate system). Data  
871 are from 08:00 to 13:00 UTC. Panels e) to j): current sheet crossing between 10:30:12 and 10:30:18. The  
872 magnetic field (panel e) is provided in the local LMN coordinate system. The Walén test is illustrated in  
873 panel f). Panel g) shows the electron pitch angle distribution for the energy 274-577eV. Panel i) show the  
874 ion plasma beta while panel j shows the electron plasma beta. The first two black lines delimit the  
875 current sheet and the second and third black lines delimit the electron boundary layer. Panels k) to o) are  
876 similar to Panels e) to j) with data between 11:07:45 and 11:07:54. The two solid black lines delimit the  
877 current sheet.

878



879

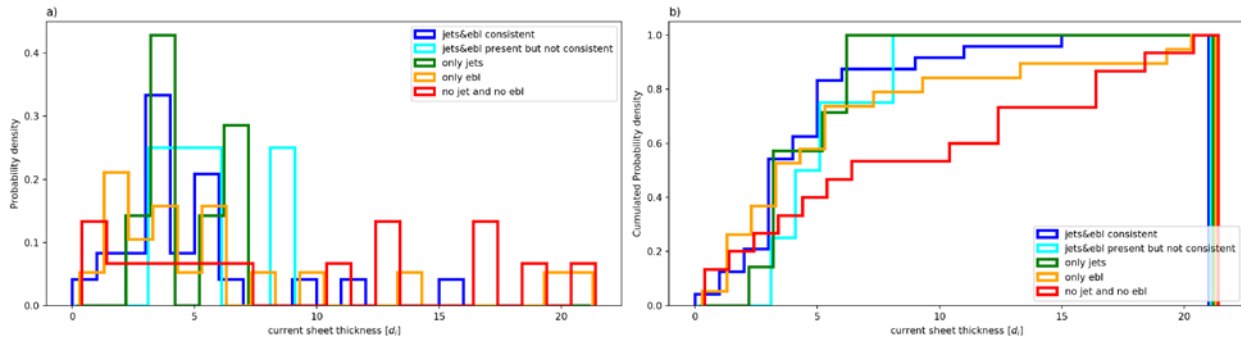
880 **Figure 4:**

881 Test of the *Swisdak et al.* [2003] model (see Equations 1, 2, and 3) for 69 current sheets crossings. The

882 first, second and third column use Equations (1), (2), and (3), respectively. First row to second to last row

883 represent likelihood of events presenting magnetic reconnection signatures. The last row gathers all  
 884 crossings at once. In each panel is represented the reconnection suppression condition for  $L_{eq}/d_i = 0.5$ ,  
 885 1, and 2 in red, black, and blue, respectively. Events which satisfy the model (i.e., where reconnection is  
 886 allowed) are expected above the curves while suppressed events should be located under the curves.

887

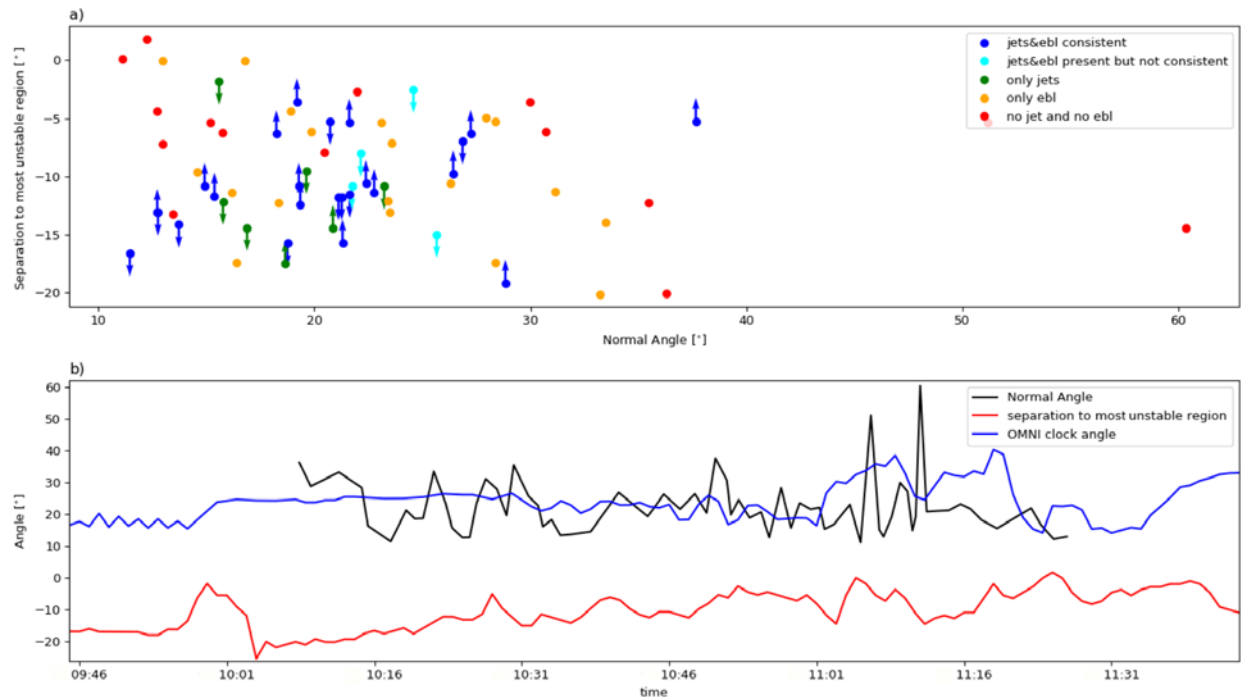


888

889 **Figure 5:**

890 Distributions of current sheet thicknesses (in inertial length) with their likelihood of being reconnecting  
 891 events. Panel a) presents the normalize distributions of thicknesses, and Panel b) presents the  
 892 cumulative distributions.

893



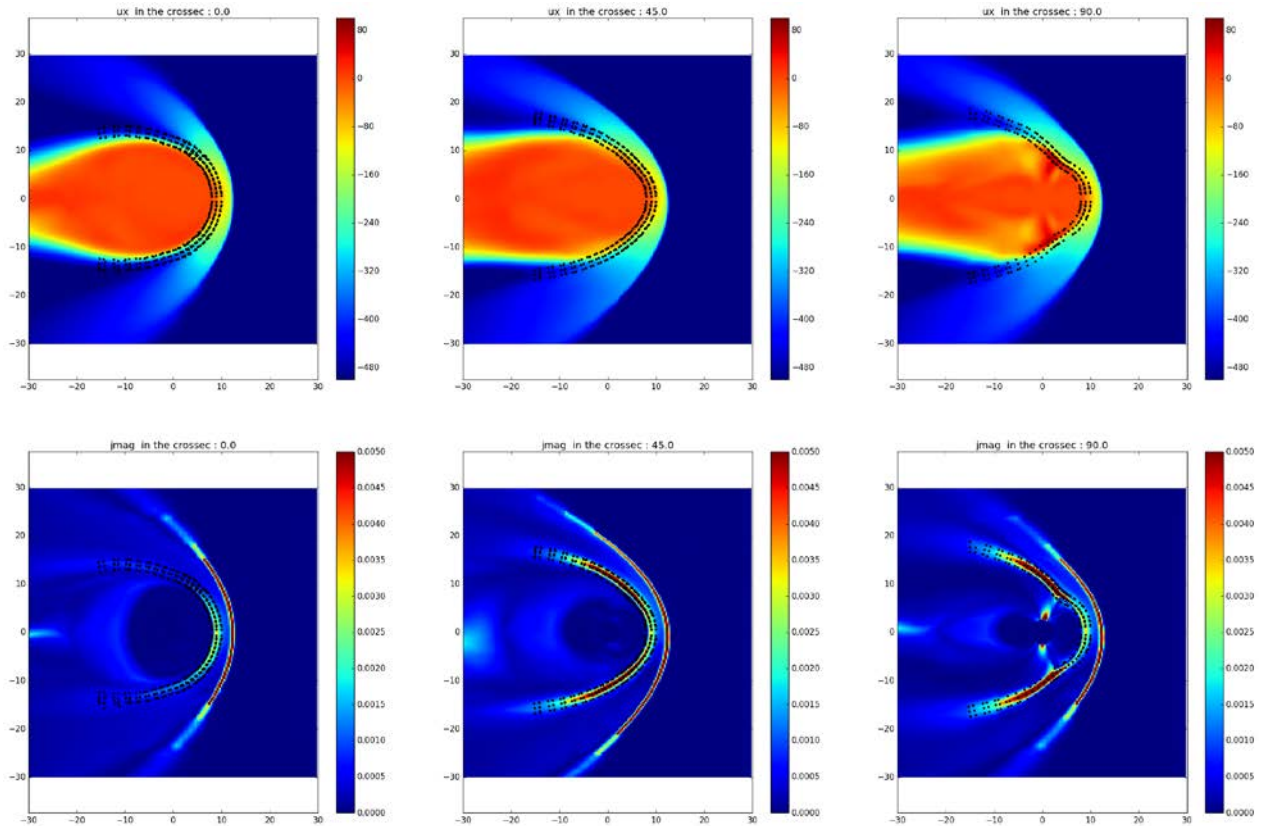
894

895 **Figure 6:**



896 Panel a: latitude distance (in degrees) between the MMS spacecraft and the most unstable plane derived  
 897 from the global MHD model as a function of the angle between the normal of each current sheet and the  
 898 normal of the unperturbed magnetopause (“normal angle”). The directionalities of the jets in accordance  
 899 with the magnetic field geometry are represented with arrows. Events are grouped by their observed  
 900 signatures. Panel b): time series during the observation of the KH instability at the magnetopause. The  
 901 panel shows the “normal angle” in black, the OMNI clock angle in blue, and the separation between the  
 902 spacecraft and the most unstable plane (in red).

903



904

905 **Figure 7**

906 Results from CCMS’s BATS’R’US simulation code. Bulk velocity and current density magnitude in two-  
 907 dimensional cuts: equatorial plane, 45° plane, and meridional plane. The scatter points represent the  
 908 magnetopause detection results with the corresponding magnetospheric and magnetosheath points.